

Máster en Física Avanzada

Especialidad en Física Nuclear y de Partículas



Trabajo Fin de Máster

Analysis of Long Lived Particles with **BuSca** at
LHCb.

Valerii Kholoimov

Tutor: Prof. María Aránzazu de Oyanguren Campos

Curso académico 2024/25

Abstract

BuSca stands for Buffer Scanner and is a LHCb project prototype designed for long-lived particle searches in real-time, leveraging the enhanced parallelization capabilities of the new LHCb trigger scheme implemented on GPUs (the Allen project). BuSca algorithms are focused at present on *downstream* reconstructed tracks, which exclusively let hits in the UT and SciFi detectors. By projecting physics candidates onto 2D histograms of flight distance and mass hypotheses at 30 MHz rate, BuSca identifies hot spots indicative of potential candidates of new particles, thereby providing strategic guidance for the development of new trigger lines. Additionally, BuSca offers an Armenteros-Podolanski representation, providing insights into the mass hypotheses of the decay products associated with the new particle. The design and performance of BuSca, including the outcomes of its initial prototype on simulated and real data, are presented in this manuscript.

Contents

1	Theoretical introduction	5
1.1	Standard Model	5
1.2	Long-living Particles (LLPs)	6
1.3	Long-Lived Particles Beyond the Standard Model	8
2	The Large Hadron Collider (LHC)	9
2.1	Experimental status of LLP searches	11
3	The LHCb experiment	12
3.1	VERTex LOcator (VELO)	13
3.2	Upstream Tracker (UT)	13
3.3	Scintillating Fibre Tracker (SciFi)	15
3.4	Magnet	16
3.5	Track description and types at LHCb	16
3.6	Track description model	17
3.7	The LHCb trigger system	18
3.7.1	High Level Trigger 1 (HLT1)	19
3.7.2	High Level Trigger 2 (HLT2)	19
3.8	Track reconstruction algorithms at HLT1	20
3.8.1	<i>VELO</i> track reconstruction	20
3.8.2	<i>SciFi</i> track reconstruction	20
3.8.3	<i>Long</i> track reconstruction	20
3.9	<i>Downstream</i> track reconstruction	21
3.9.1	Track reconstruction	21
3.9.2	Performance of the algorithm	22
3.9.3	Physics efficiency	23
3.9.4	Downstream vertexing	23
3.10	Studies of sensitivity to BSM particles	24
3.10.1	BC4 and BC5 Scalar Boson Models	24
4	BuSca framework	26
4.1	BSM particle simulations	27
4.2	Selection	27
4.3	LHCb HLT1 monitoring system	28
4.4	BuSca histograms	29
4.4.1	Mass versus Flight Distance	29
4.4.2	Armenteros-Podolanski plot	31
4.4.3	Helicity versus Mass histogram	32

4.4.4	High Mass monitoring	33
4.5	BuSca selection lines	34
4.6	BuSca performance impact	34
4.7	Background studies	35
4.7.1	Hadronic resonances	35
4.7.2	Strange candidates	37
4.7.3	Combinatorial background	37
4.8	BuSca results using 2024 data	38
4.9	Application for detecting incorrect reconstruction	39
4.10	Prospects	40
5	Conclusions	41
	References	42

Acknowledgments

First and foremost, I would like to express my sincere gratitude to my supervisor, Arantza Oyanguren Campos, for her invaluable guidance, continuous support, and insightful feedback throughout the course of this thesis. Her expertise and encouragement have been essential to the successful completion of this work.

I also want to thank the members of the IFIC-LHCb group for their insights, ideas, stimulating discussions and help throughout my work: Brij, Fernando, Izaac, Jiahui and Volodymyr.

I would like to express my sincere gratitude to Andrii Usachov and Maksym Ovchynnikov for their valuable guidance and generous support throughout my research. Their deep insights into the capabilities of the LHCb detector and its sensitivity to rare processes beyond the Standard Model were essential in shaping the direction of this work. Our discussions on optimizing experimental strategies and improving analysis techniques provided clarity and inspiration during key phases of the project. It has been a privilege to learn from their expertise.

I am deeply grateful to my family for their unwavering support, patience, and love throughout my academic journey. Your belief in me has been a constant source of motivation.

Lastly, I acknowledge the support of Institute for Research and Innovation in Software for High Energy Physics (IRIS-HEP), whose resources and assistance made this research possible.

Thank you all.

1 Theoretical introduction

1.1 Standard Model

The Standard Model (SM) is currently the leading theory in particle physics, providing a comprehensive framework for understanding the fundamental components of matter and their interactions. It successfully explains three out of the four known fundamental forces: electromagnetic, strong, and weak forces, but does not address gravity, which is covered by general relativity. Within the SM, all matter is composed of two types of spin-1/2 particles - quarks and leptons - collectively known as fermions. Quarks combine to form protons and neutrons, the parts of atomic nuclei, and other heavier particles, whereas leptons include particles like electrons and neutrinos. The Standard Model organizes all known elementary particles according to their fundamental properties. In Fig. 1, a summary table of the known fundamental particles of the SM is illustrated.

mass →	$\approx 2.3 \text{ MeV}/c^2$	$\approx 1.275 \text{ GeV}/c^2$	$\approx 173.07 \text{ GeV}/c^2$	0	$\approx 126 \text{ GeV}/c^2$
charge →	$2/3$	$2/3$	$2/3$	0	0
spin →	$1/2$	$1/2$	$1/2$	1	0
	u up	c charm	t top	g gluon	H Higgs boson
QUARKS	$\approx 4.8 \text{ MeV}/c^2$ $-1/3$ $1/2$	$\approx 95 \text{ MeV}/c^2$ $-1/3$ $1/2$	$\approx 4.18 \text{ GeV}/c^2$ $-1/3$ $1/2$	0 0 1	
	d down	s strange	b bottom	γ photon	
	$0.511 \text{ MeV}/c^2$ -1 $1/2$	$105.7 \text{ MeV}/c^2$ -1 $1/2$	$1.777 \text{ GeV}/c^2$ -1 $1/2$	$91.2 \text{ GeV}/c^2$ 0 1	
	e electron	μ muon	τ tau	Z Z boson	
LEPTONS	$< 2.2 \text{ eV}/c^2$ 0 $1/2$	$< 0.17 \text{ MeV}/c^2$ 0 $1/2$	$< 15.5 \text{ MeV}/c^2$ 0 $1/2$	$80.4 \text{ GeV}/c^2$ ± 1 1	W W boson
	ν_e electron neutrino	ν_μ muon neutrino	ν_τ tau neutrino		GAUGE BOSONS

Figure 1: Particle content of the Standard Model [1]

Fermions are grouped into three generations, each containing a pair of quark with distinct electric and flavor charges, and two types of leptons. In addition, the table lists the spin-1 gauge bosons that mediate the fundamental forces, as well as the scalar Higgs boson. Every particle has an antiparticle with the same mass but opposite conserved quantum numbers. Particles like the Z and γ bosons, which have no charge, are their own antiparticles.

Forces between particles are mediated by the exchange of bosons with spin 1. The

electromagnetic interaction is carried by photons, while the weak force is transmitted by the W^\pm and Z bosons. These two forces are unified at a fundamental level and are collectively known as the electroweak (EW) force. In contrast, the strong interaction, which binds quarks together inside hadrons (such as protons and neutrons), is mediated by gluons. The theoretical framework describing quark and gluon dynamics is called Quantum Chromodynamics (QCD).

The Higgs boson, the latest particle discovered within the Standard Model, is essential for understanding how fundamental particles acquire mass [2, 3]. Its characteristics have been measured at the Large Hadron Collider (LHC) at CERN, and current results show agreement with the Standard Model's expectations.

Quarks, which are among the basic building blocks in the SM, can combine in various configurations to create composite particles. For example, baryons—such as protons and neutrons—are composed of three quarks, while mesons are formed from a quark paired with an antiquark. The SM itself is constructed as a relativistic Quantum Field Theory (QFT) [4], where different quantum fields extend throughout space-time. The particles we observe are excitations of these fields, and their interactions correspond to the fundamental forces. These interactions are mathematically described by the Lagrangian:

$$\mathcal{L}_{\text{SM}} = \mathcal{L}_{\text{EW}} + \mathcal{L}_{\text{QCD}} + \mathcal{L}_{\text{Higgs}} + \mathcal{L}_{\text{Yukawa}}, \quad (1.1)$$

where the terms represent, in order, the electroweak (EW) and strong (QCD) forces, the Higgs sector, and the Yukawa interactions, which describe how the Higgs field couples to fermions. The Higgs field gives mass to the Z and W^\pm bosons and fermions through spontaneous symmetry breaking [5, 6].

Despite its many achievements, the SM leaves several important questions unanswered. It does not provide explanations for dark matter or dark energy, and it cannot be reconciled with general relativity, which describes gravity—partly due to the absence of experimental evidence for the graviton*. The observed dominance of matter over antimatter in the Universe also remains a puzzle that the SM cannot resolve.

These open questions motivate the ongoing search for new physics beyond the Standard Model (BSM), with the goal of achieving a deeper understanding of the Universe and possibly unifying all known forces. Many BSM scenarios predict the existence of so-called "long-lived particles", which will be discussed in the next section.

1.2 Long-living Particles (LLPs)

The mean lifetime τ of an unstable particle quantifies the average duration for which it exists before decaying. This quantity is the inverse of the decay width, $\tau = 1/\Gamma$, where the width Γ represents the probability per unit time that the particle transforms into a

*A hypothetical fundamental particle with spin 2 that is proposed to mediate the force of gravity.

given set of final states. When multiple decay channels are available, the total width is simply the sum of the partial widths, $\Gamma = \sum_i \Gamma_i$, with i labeling each specific channel.

The size of the decay width depends on several factors: the masses and quantum numbers of the particles involved, the interaction strength, and the phase space that is kinematically accessible. The probability that a particle decays after a time interval t is

$$P(t) = 1 - e^{-\Gamma t}.$$

Stronger interactions—such as the strong nuclear or electromagnetic forces—typically lead to shorter lifetimes.

The lifetimes of most Standard Model particles are incredibly short, often around 10^{-25} s. In contrast, a select few, including the electron and proton, are effectively stable, with the proton having a potential lifetime of up to 10^{35} yr. Figure 2, adapted from Refs. [7, 8], situates selected SM particles on the lifetime–mass plane and divides them into three regions: prompt decaying states ($c\tau < 1 \mu\text{m}$), particles that decay and produce displaced vertices experimentally accessible ($1 \mu\text{m} < c\tau < 10 \text{ m}$), and particles that appear stable to a detector ($c\tau > 10 \text{ m}$).

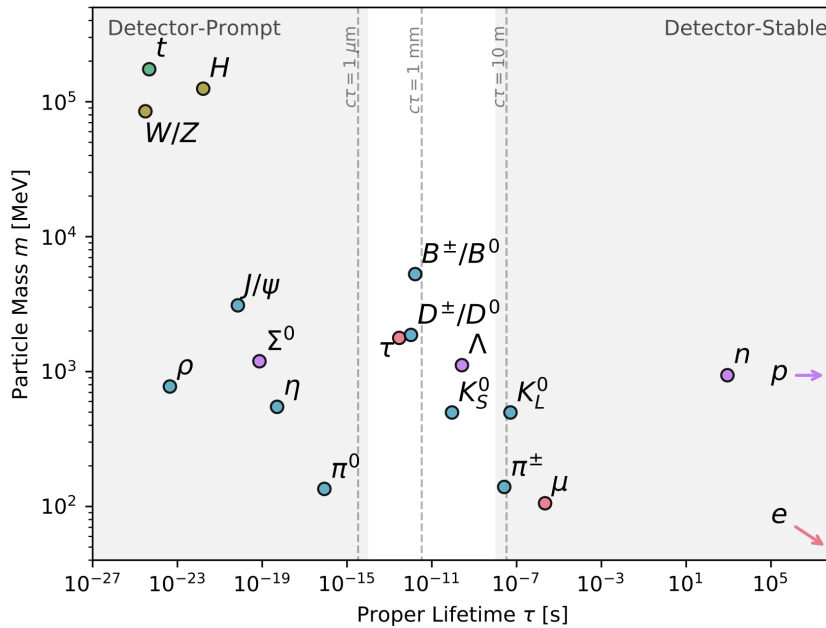


Figure 2: Illustration of several SM particles in the lifetime–mass plane. The plot is subdivided into three zones: prompt particles ($c\tau < 1 \mu\text{m}$), particles whose decays may yield displaced vertices ($1 \mu\text{m} < c\tau < 10 \text{ m}$), and particles regarded as stable by the detector ($c\tau > 10 \text{ m}$) [8].

Because lifetimes span so many orders of magnitude, the expression “long-lived particle” is inherently context-dependent. In proton–proton collider experiments—and for the purposes of this work—particles with lifetimes of roughly 100 ps or longer are termed long-lived. Within the SM, this definition mainly encompasses the strange hadrons K_S^0 and Λ^0 .

In many BSM theories, small couplings between an LLP and lighter states can likewise give rise to extended lifetimes. Several such scenarios will be outlined in the next section. For the present study, the geometric acceptance of the LHCb detector is a key factor in defining the lifetime range to which the experiment is sensitive.

1.3 Long-Lived Particles Beyond the Standard Model

Particles with extended lifetimes arise in numerous theories beyond the Standard Model. In many cases these states interact only feebly with ordinary matter, making them exceptionally difficult to detect. Moreover, long-lived particles are of great interest to cosmology—they can shed light on dark-matter phenomena and may play a role in early-Universe processes such as leptogenesis and baryogenesis [9]. For an LLP of mass m that decays through a heavy off-shell mediator of mass M , the decay width can be approximated by

$$\Gamma \sim \frac{\epsilon^2}{(8\pi)^{a-1}} \frac{m^n}{M^{n-1}}, \quad (1.2)$$

where ϵ is a (potentially very small) coupling, n is a positive integer fixed by the underlying model, and a denotes the number of particles in the final state. A wide variety of LLP scenarios has been proposed. In the following, several representative BSM frameworks that predict LLPs are briefly outlined. In this work we adopt the benchmark cases recommended by the Physics Beyond Colliders (PBC) working group [10], labelled as *BCX*:

1. **Dark photons V (*BC1*).** These vector bosons couple to the SM hypercharge gauge field via kinetic mixing. Below the electroweak scale the interaction strength is governed by the parameter ϵ . The production mechanisms and decay modes used here follow Refs. [11, 12].
2. **Higgs-like dark scalars S .** Beneath the electroweak scale Λ_{EW} , their interactions are set by the scalar–Higgs mixing angle $\theta^\dagger \ll 1$ and the coupling α of the hSS operator. In *BC4* we take $\alpha = 0$, whereas *BC5* fixes α such that $\text{Br}(h \rightarrow SS) = 0.01$. The phenomenology follows Ref. [13]. Unlike earlier studies that used an inclusive $b \rightarrow s + S$ approximation [10, 14], Ref. [13] employs an exclusive description based on specific B -meson channels, which remains valid for $m_S \gtrsim 2\text{--}3 \text{ GeV}/c^2$.
3. **Heavy Neutral Leptons N .** We consider mixing with each active neutrino flavour: ν_e (*BC6*), ν_μ (*BC7*), and ν_τ (*BC8*). Below Λ_{EW} their interactions are governed by the mixing parameters U_α . This implementation is based on Ref. [15], transitioning

[†] θ is the scalar mixing angle arising from mass mixing between the Higgs boson h and a beyond Standard Model scalar S after electroweak symmetry breaking, where the interaction $h \rightarrow h + \theta S$ leads to suppressed couplings of S to Standard Model particles.

from an exclusive meson-level treatment of semileptonic decays to an inclusive quark-level approach.

4. **Axion-like particles (ALPs).** Defined at a scale $\Lambda_{\text{ALP}} > \Lambda_{\text{EW}}$, ALPs can couple to Chern–Simons densities of gauge fields or to fermionic axial currents. In *BC10* the ALP couples universally to fermion axial currents; in *BC11* it interacts with the gluonic Chern–Simons operator. Production and decay channels follow Ref. [16]. For *BC10* this includes modes omitted in earlier work [10]; for *BC11* the decay-width prescription differs from Ref. [17], yielding larger widths and therefore shorter lifetimes (see Ref. [16] for details).

Reference [18] compiles the dominant LLP production and decay mechanisms relevant to high-energy experiments. LLPs can emerge directly in proton–proton collisions, from decays of Standard Model hadrons or gauge bosons, or via mixing with light neutral mesons—processes that are particularly pertinent for LHCb. For completeness, the channels considered in this study are listed in Table 1. Of special interest for this work are those decaying into two tracks, independently of the production mechanism.

Model	Production	Decay modes
Dark scalar [S]	$B_{(s)} \rightarrow SX_s$ $B \rightarrow SSX$ $h \rightarrow SS$	$\ell^+\ell^-, \pi^+\pi^-,$ $K^+K^-, c\bar{c}, gg\dots$
Heavy lepton [N]	$B/D \rightarrow NX$ $W \rightarrow N + \ell$	$\ell q\bar{q}', \nu q\bar{q}$ $\nu\ell\ell', \dots$
Massive photon [V] U_{B-L} mediator	$\pi/\eta/\eta' \rightarrow VX$ Bremsstrahlung Drell-Yan	$\ell^+\ell^-, \pi^+\pi^-,$ $\pi^+\pi^-\pi^0, K^+K^-$
Axion-Like-Particle [a]	$B_{(s)} \rightarrow aX_s$ $\pi^0/\eta/\eta'$ mixing Drell-Yan	$\ell^+\ell^-, \eta 2\pi, 4\pi$ gg

Table 1: Summary of the production and decay modes of the LLPs considered in this work. Here, X denotes any SM particle.

2 The Large Hadron Collider (LHC)

The Large Hadron Collider is situated approximately 100 m underground at the CERN site near Geneva, Switzerland. Spanning a 27-kilometer tunnel, it stands as the world’s most powerful particle accelerator. After the first proton-proton collision at a $\sqrt{s} = 7$ TeV was delivered in 2009, it collected data during the first data-taking period, Run 1 from 2009 to 2012, reaching a peak energy of $\sqrt{s} = 8$ TeV. It then continued during the second data-taking period, Run 2 from 2015 to 2018, with a collision energy of $\sqrt{s} = 13$ TeV, 1 TeV below the design energy, alternating protons and ions, mainly lead, beams. After the conclusion of the second long shutdown in 2022, the Run 3 data-taking is now taking

place, operating with 6.8 TeV beams, and it is foreseen to conclude in 2025 to allow the upgrade of the LHC machine in order to provide higher intensity beams. In Fig. 3) the schedule of the LHC and High luminosity upgrade (HL-LHC) is shown.

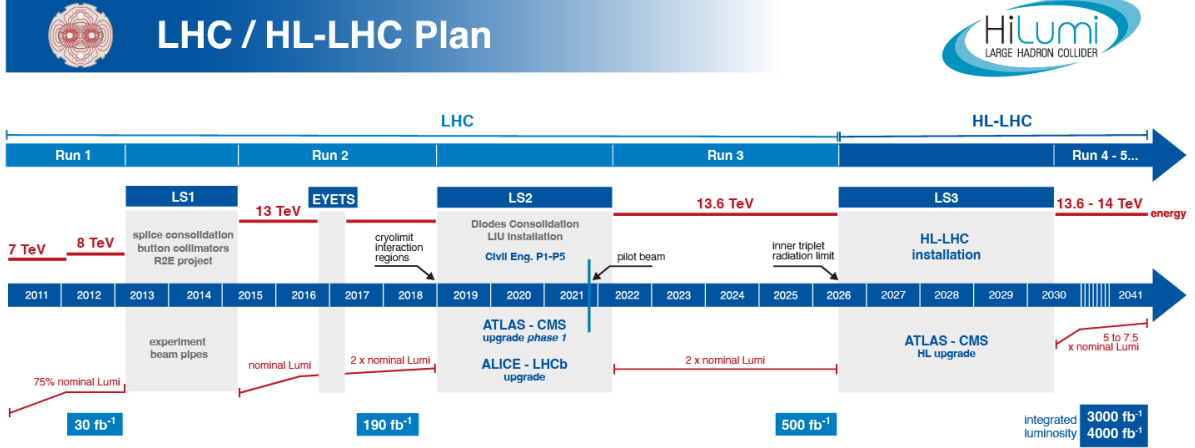


Figure 3: Schematic representation of the operation time schedule of LHC. [19].

Each LHC beam can accommodate up to approximately 2800 proton bunches, with each bunch containing roughly 1.15×10^{11} protons. The instantaneous luminosity, L_{inst} , which determines the collision rate, is expressed as

$$L_{\text{inst}} = \frac{N^2 f n_b}{4\pi\sigma_x\sigma_y},$$

For the LHCb experiment, which is the focus of this study, the integrated luminosities collected are approximately 3 fb^{-1} in Run 1, 6 fb^{-1} in Run 2, and 15 fb^{-1} (partial) for July 2025 in Run 3.

Another critical parameter is the average number of interactions per bunch crossing, known as *pile-up* and denoted μ :

$$\mu = \frac{L_{\text{inst}} \sigma_{\text{inel}}}{f},$$

where $\sigma_{\text{inel}} \approx 80 \text{ mb}$ at 14 TeV is the inelastic pp cross-section. Maintaining a manageable pile-up is essential for event reconstruction; typical values at LHCb are $\mu \approx 1.1$ in Run 1, $\mu \approx 1.5$ in Run 2, and approximately $\mu \approx 5.3$ in Run 3.

Figure 4 sketches the LHC accelerator complex and indicates the principal experiments. Four main detectors are located at different interaction points around the ring, each designed for a specific physics program. ATLAS and CMS are general-purpose detectors capable of a wide range of searches, including the Higgs boson discovery. ALICE is optimized for studying quark-gluon plasma through heavy-ion (lead-lead) collisions. LHCb focuses on flavor physics, examining the decays of b - and c -quark hadrons, matter-antimatter asymmetries, and hadron spectroscopy.

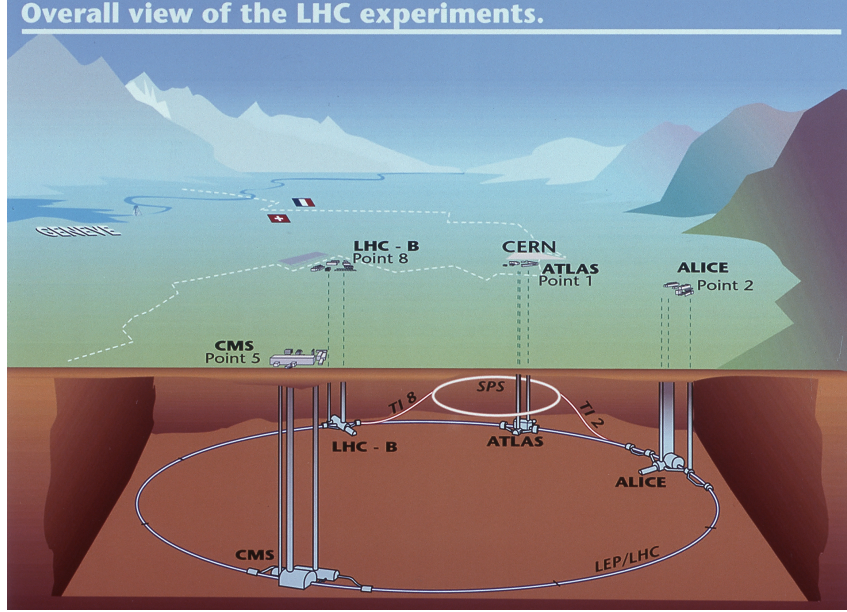


Figure 4: Schematic view of the LHC complex and its major experiments [20].

2.1 Experimental status of LLP searches

The LHCb collaboration has investigated long-lived particles using pp data recorded in Run 1 (2011–2012) and Run 2 (2015–2018). These studies explored a range of topologies, including:

- a single lepton emerging from a high-multiplicity displaced vertex [21],
- pairs of spatially separated displaced vertices, each with many outgoing tracks [22, 23],
- B -meson decays proceeding via a Majorana neutrino and yielding two same-sign leptons produced at different vertices [24, 25],
- B -meson decays that reconstruct two opposite-charge leptons in a displaced vertex [26, 27],
- heavy, charged, quasi-stable tracks reaching the muon stations but moving below the Cherenkov threshold of the RICH [28],
- prompt muons that combine to form a high-quality displaced vertex [29].

The general-purpose detectors ATLAS and CMS have also conducted extensive searches for long-lived particles. Their programmes encompass a variety of signatures, including displaced muons, non-pointing photons, displaced di-electromagnetic vertices (such as $H \rightarrow \gamma\gamma$ or $Z \rightarrow e^+e^-$), jets that are either trackless or time-delayed, and multiply charged particles.

To date, the majority of new physics searches have concentrated on promptly decaying states—particles that decay near the interaction point, allowing their decay products to traverse the full detector. New experimental approaches are being developed to enhance sensitivity to particles with much longer lifetimes. In addition to planned upgrades for ATLAS, CMS, and LHCb, several dedicated experiments have been proposed, including MoEDAL–MAPP [30], MATHUSLA [31], CODEX-b [32], FASER [33], and SHiP [34]. A comprehensive overview of current results and future prospects is provided in Ref. [35].

This work focuses on an upgraded configuration of LHCb designed to search for BSM particles with lifetimes greater than approximately 100 ps.

3 The LHCb experiment

The LHCb forward spectrometer, shown in Fig. 5, is one of the main detectors at the LHC accelerator at CERN, primarily targeting the search for new physics through the study of CP-violation and heavy-flavor hadron decays. It has been operational throughout all LHC Runs (Run 1 - Run 3) with exceptional performance, recording an integrated luminosity of 24 fb^{-1} for now at center-of-mass energies of 7, 8, and 13 TeV, and has contributed to numerous precise physics results and the discovery of new particles [36].

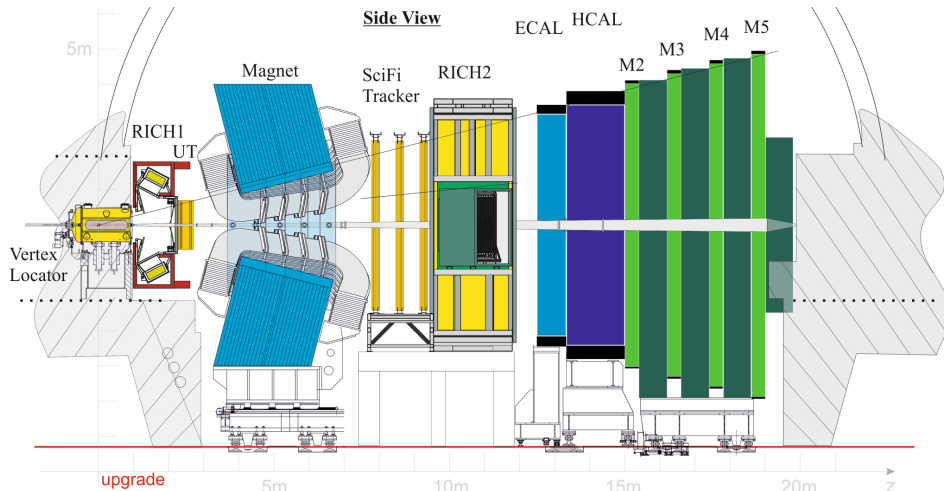


Figure 5: The LHCb detector operating during the Run 3 [37].

The LHCb experiment has undergone a major transformation, with its detectors almost completely replaced. This upgrade allows it to operate at an instantaneous luminosity five times higher than before. The first level software trigger executed on Graphic Processor Units (GPU) represents one of the main features of the new LHCb design [37], allowing the reconstruction and selection of events in real-time and widening the physics reach of the experiment [38]. The primary features of the new LHCb detector are outlined in [39] and summarized below. Compared to the previous detector [40], one of the most significant enhancements is related to the new tracking system, which, together with the

new trigger scheme, is crucial for this work.

The detector subsystems of LHCb are:

1. **Tracking detectors:** they measure the momenta of charged particles and identify the collision and decay vertices. To effectively conduct heavy flavor measurements, excellent vertex and proper time resolution are necessary, along with precise invariant mass reconstruction. The LHCb tracking system consists of VERTex LOCator (VELO), Upstream Tracker (UT), and Scintillating Fiber Tracker (SciFi).
2. **A dipole magnet:** which bends the trajectory of charged particles and enables momentum measurements.
3. **Particle Identification (PID) system:** supplies information on the speed and/or energy of particles, which, when combined with momentum data, enables the identification of various charged particle species and some neutral particles, such as photons and neutral pions. Specifically, exceptional π -K-p separation is necessary to distinguish rare b -physics signal events from background noise.

3.1 VERTex LOCator (VELO)

The VELO detector is responsible for reconstructing primary and secondary vertices and measuring track positions near the interaction point (IP). Its spatial resolution is finer than the typical decay lengths of b - and c -hadrons, i.e., $c\tau \approx 0.01$ cm to 1 cm, which is essential for effectively rejecting background from heavy flavor signals. During Run 2, the detector was composed of silicon micro-strip layers, and it has been upgraded to silicon hybrid pixel technology for Run 3.

The core technology of the new VELO consists of pixelated hybrid silicon sensors with $55\ \mu\text{m} \times 55\ \mu\text{m}$ dimensions, arranged into 52 modules with four sensors each, and cooled by a bi-phase CO_2 microchannel system embedded in the silicon substrate. The VELO services have been redesigned to reduce both the material budget and the inner radius along the beamline. The modules are organized into two movable halves, Side C ($x < 0$) and Side A ($x > 0$). Both sides share a common z distribution, but the C-side modules are shifted by 12.5 mm along the z axis to ensure mechanical compatibility and sensor overlap when closed, providing complete azimuthal coverage. A sketch of the VELO detector is shown in Fig. 6.

3.2 Upstream Tracker (UT)

The second tracker in LHCb, named Upstream Tracker (UT) is positioned between the RICH1 detector and the dipole magnet. It plays a critical role in charged-particle tracking [41]. The setup comprises four planes of silicon strip detectors and it is shown in Fig. 7. The planes are referred to as UTaX, UTaU, UTbV and UTbX. The strips in UTaX and

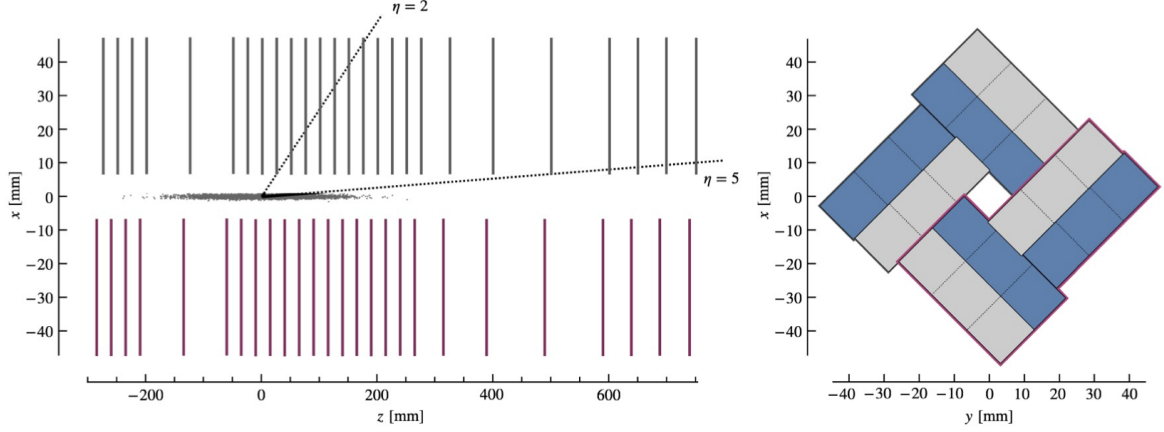


Figure 6: Left: A top-view on the $z-x$ plane at $y=0$ shows the luminous region z -extent and pseudorapidity acceptance ($2 < \eta < 5$). Right: A sketch presents the ASICs' standard layout around the z -axis in the closed VELO. ASICs are split between the upstream (grey) and downstream (blue) module faces. Side C modules are highlighted in purple in both images.

UTbX plane are arranged vertically along the y -axis and in UTaU and UTbV are inclined at stereo angles of 5° .

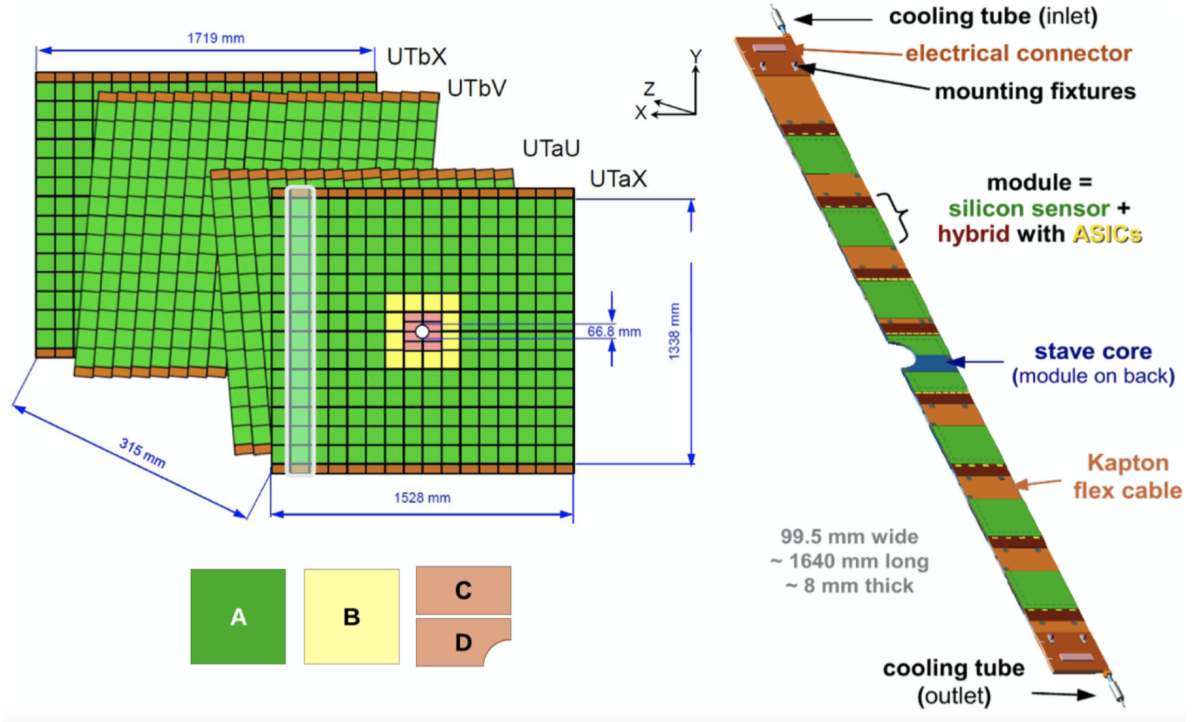


Figure 7: The configuration of the UT's four layers is illustrated. Distinct colors represent the various sensor types. On the right, the design of a UT stave is displayed [42].

The UT provides a preliminary momentum estimation for tracks with transverse momentum $p_T > 0.2$ GeV/c, by using fringe magnetic field between the interaction region and the UT itself. This results in moderate precision ($\approx 15\%$) which allows to expedite the matching with Scintillating Fibre Tracker (SciFi) hits. Furthermore, the UT provides

essential information about particles that decay after the VELO such as the long-lived K_S^0 and Λ . The UT is one of the most important detectors for this work. It was installed and operational at the end of 2024 due to delays in the construction.

3.3 Scintillating Fibre Tracker (SciFi)

The Scintillating Fibre Tracker (SciFi), the farthest LHCb tracker and the most innovative detector of the LHCb upgrade, is placed downstream of the LHCb dipole magnet as shown in Fig. 8. It uses the cutting-edge technology of long scintillating fibers. The detector is responsible for charged particle tracking and momentum estimation.

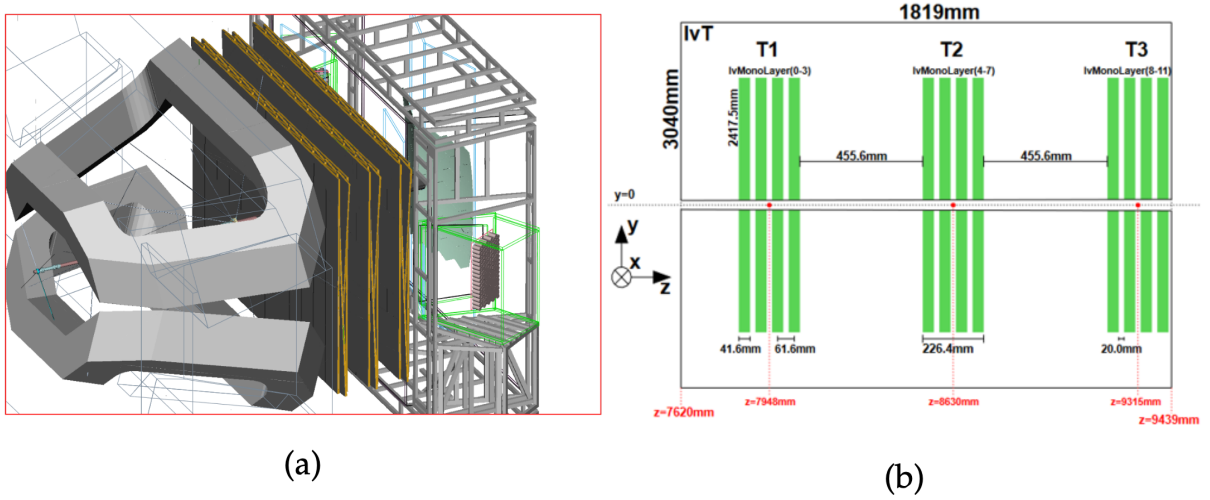


Figure 8: (a) The three stations of the SciFi are shown between the dipole magnet on the left and RICH2 on the right. (b) Sketch of the SciFi detector showing the three stations and the four layers in each station.

To meet the nominal LHCb acceptance, the tracker has to cover an area of roughly $6\text{ m} \times 5\text{ m}$ in the $x - y$ plane. The acceptance of the new SciFi detector ranges from approximately 20 mm from the beam pipe edge to distances of $\pm 3186\text{ mm}$ and $\pm 2425\text{ mm}$ in the horizontal and vertical directions, respectively. The detector relies on $250\text{ }\mu\text{m}$ diameter plastic scintillating fibers in multi-layered fiber mats, arranged in 12 detection planes across 3 stations (named T1, T2, T3) with four layers in an $x - u - v - x$ configuration. Such configuration means that the detection layers are oriented at (0 deg, +5 deg, -5 deg, 0 deg) relative to the vertical axis, which allows the determination of the particle trajectories in both x and y coordinates.

The stations are built from identical SciFi modules that are approximately 52 cm wide, spanning the full height. Figure 8 shows a sketch of the different stations. Each station has four layers with each layer having two independently movable structures, referred to as C-frames, on either side of the beam pipe. The scintillating fibers light signals are detected by 128-channel arrays of silicon photomultipliers (SiPM) with a channel pitch of $250\text{ }\mu\text{m}$.

3.4 Magnet

A dipole magnet, located between the UT and SciFi, induces a deviation in particle trajectory in the horizontal plane from which it is possible to extract its momentum. The integrated magnetic field between the UT and SciFi is 4 Tm.

The polarity of the magnet is reversed periodically to minimize possible systematic uncertainties due to the detector asymmetries, which average out by using each half of the data in a different configuration (i.e magnet polarity up and down). The magnetic field distribution is shown in Fig. 9.

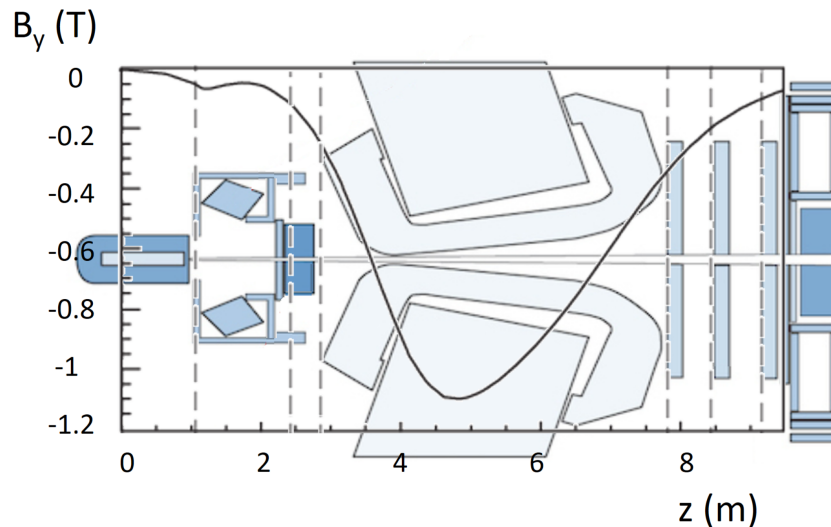


Figure 9: Distribution of the LHCb magnetic field as function of z . The VELO, RICH1, UT, magnet and the SciFi are superimposed.

3.5 Track description and types at LHCb

The existing convention on track types is based on the particular subdetectors the particle flies through. The main types are shown in Fig. 10, and are defined as

- **Upstream tracks** - formed by particles that pass through VELO and UT but do not reach SciFi.
- **Long tracks** contains hits from at least VELO and SciFi subdetectors. Presence of UT hits is optional. These are the main tracks used in physics analyses and at all stages of the trigger.
- **Downstream tracks** usually formed by decay products of K_S^0 and Λ particles, as they require only hits in UT and SciFi but not VELO. Recently, the reconstruction of these tracks was implemented at HLT1 level [43].
- **T tracks**: they only have hits from the SciFi. They are typically not included in physics analysis. Nevertheless, their potential for physics has been recently

probed [44].

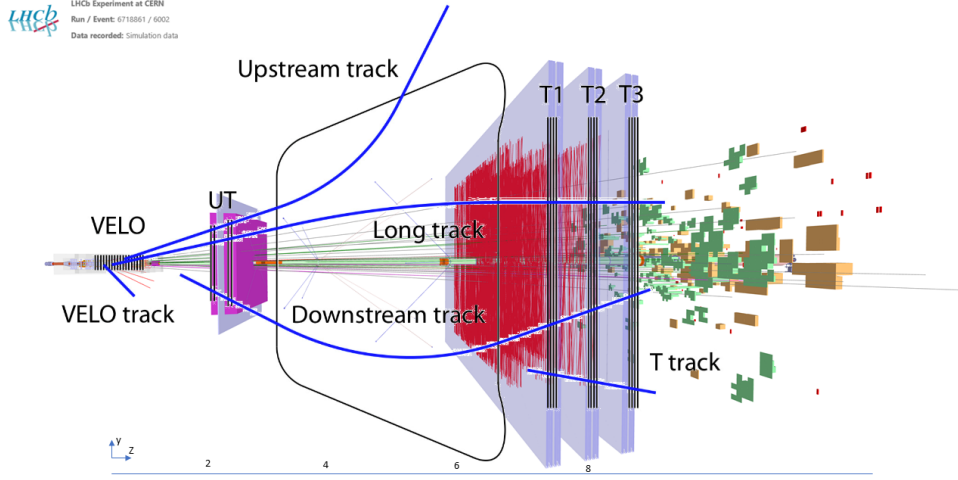


Figure 10: LHCb track types shown as blue lines. The LHCb tracking detectors together with example calorimeter clusters are superimposed.

In LHCb, the coordinate system is adopted for the tracking system and is right-handed with axes denoted as x , y , and z :

- The z -axis is collinear with the beam pipe, originating at the collision point and extending through the detector.
- The x -axis, perpendicular to the z -axis, lies in the plane where charged particles deviate due to the magnetic field, termed as the bending plane or the $x - z$ plane. The axis is pointed towards the outside of the LHC ring.
- The y -axis is orthogonal to both the x and z axes, pointing upwards, and defines the non-bending plane, referred to as the $y - z$ plane.

3.6 Track description model

Particle tracks are represented as a series of linear segments, with each segment referred to as a track state, defined at a specific z . This approach assumes that over short distances, the track can be approximated as a straight line, despite the curvature caused by the magnetic field. Each track state is characterized by a five-dimensional state vector, \vec{s} , and an associated covariance matrix. The state vector is defined as:

$$\vec{s} = \begin{bmatrix} x \\ y \\ t_x \\ t_y \\ \frac{q}{p} \end{bmatrix},$$

where x and y denote the positions along the horizontal and vertical directions, respectively. t_x and t_y are the tangents of the direction angles with respect to the z coordinate, defined as $t_x = \frac{\partial x}{\partial z}$ and $t_y = \frac{\partial y}{\partial z}$. The quantity $\frac{q}{p}$ represents the charge-to-momentum ratio, where q is the charge and p is the momentum of the particle.

The covariance matrix, a 5×5 matrix, captures the uncertainties and correlations of the state vector components and is essential for track fitting and analysis. This fundamental track model provides a consistent representation of track states across the various tracking systems of LHCb.

3.7 The LHCb trigger system

The trigger system is completely renewed for Run 3 due to the inability to meet the physics requirements with the setup used in previous runs [37]. It includes the removal of the hardware trigger, and the development of brand-new software-based trigger system (shown in Fig. 11) that allows the real-time reconstruction of all events at a visible interaction rate of 30 MHz and reduced data volume from 4 TB/s down to ≈ 10 GB/s, which is suitable for permanent offline storage.

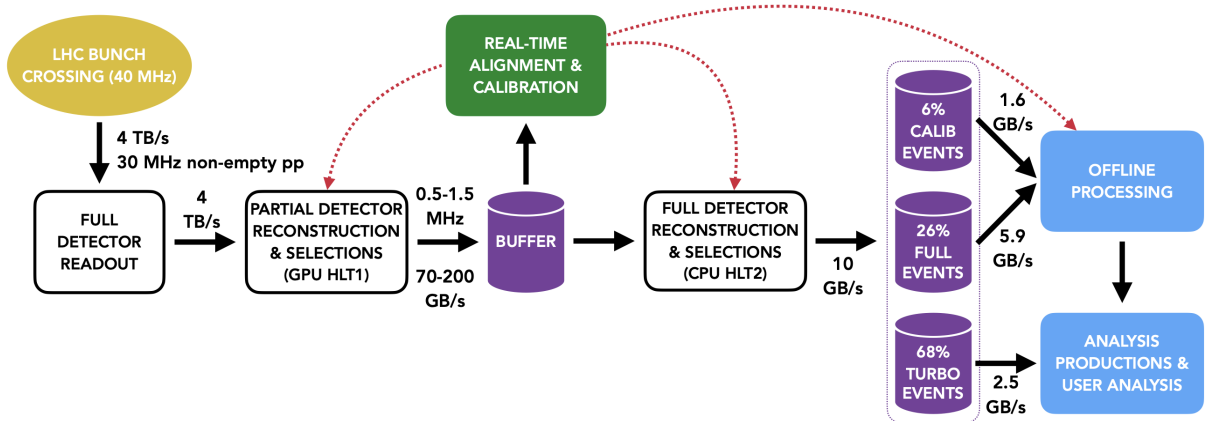


Figure 11: LHCb upgrade dataflow focusing on the real-time aspects [45].

The high rate of potentially interesting signals that can be at least partially reconstructed within the detector acceptance significantly complicates the reduction (400 times) of data flow. The trigger must fully reconstruct and pinpoint specific signals of interest, retaining only a select portion of the event's information [46]. This necessitates that the trigger executes an offline-quality reconstruction, achieved by a near real-time alignment and calibration of the detector. The LHCb real-time analysis approach, initiated in Run 2 [47], underscores this demand [48].

3.7.1 High Level Trigger 1 (HLT1)

The HLT1 level has to be executed at a 30 MHz rate and, as such, suffers from heavy constraints on timing for event reconstruction. It performs partial event reconstruction in order to reduce the data rate. Tracking algorithms play a key role in fast event decisions, and the fact that they are inherently parallelisable processes suggests a way to increase trigger performance. The HLT1 has been implemented on a number of GPUs within the **Allen** software project [49], which allows to manage 40 Tbits/s raw data rate from the upgraded LHCb detector and reduces it by a factor of 30. After this initial selection, data is passed to a buffer system, which allows a real-time calibration and alignment of the detector usually within a few minutes. This is used for the full and improved event reconstruction carried out by HLT2.

The event signal rates are predominantly driven by c -hadrons at nearly 1 MHz and b -hadrons at 300 kHz, both of which can be partially reconstructed within the LHCb's acceptance parameters. Additionally, The LHCb physics program, including electroweak physics, quarkonia, semileptonic, and rare heavy decays, among others, significantly influences the event rate. The HLT1 design ensures its output rate does not theoretically surpass 2 MHz. Yet, practical constraints, such as the disk buffer capacity and HLT2 processing speeds, dictate this rate, as visualized in Fig. 11.

In Run 2, due to timing constraints, the LHCb implementation in the HLT1 stage was based on partial reconstruction and focuses solely on *long* tracks, i.e., tracks that have hits in the VELO. This design did not allow for effectively triggering long-lived particles, significantly affecting their possible studies.

3.7.2 High Level Trigger 2 (HLT2)

The primary function of HLT2 is to carry out the full offline-quality reconstruction and selection of physics signatures. A sizable disk buffer is placed between HLT1 and HLT2 to serve as a temporary repository for data while real-time alignment and calibration are conducted. At HLT2, the fate of an event, whether it should be conserved, is determined by roughly $\mathcal{O}(1000)$ selection algorithms, each individually tuned for a distinct signal topology or physics analysis. These algorithms also decide which components of the full event are to be saved to permanent storage. The reconstruction pipeline comprises four core components: charged particle pattern recognition, calorimeter reconstruction, particle identification, and a Kalman fit for tracking. To achieve the required computing throughput, tracks, neutral objects, and particle identification data are grouped into Structure-of-Array (SoA) data structures, enabling efficient parallel processing. Selection algorithms employ both rectangular-cut-based methods and techniques rooted in multivariate analysis or artificial intelligence.

3.8 Track reconstruction algorithms at HLT1

The existing track reconstruction algorithms at HLT1 are described in the following subsections. The first two, named *VELO* and *SciFi* track reconstruction, are designed to reconstruct track segments based only on the hit information in respective detectors. While *long* and *downstream* track reconstruction algorithms combine track segments from different sub-detectors in order to reconstruct a complete particle trajectory within LHCb.

3.8.1 *VELO* track reconstruction

As a first detector around the interaction point, VELO has to deal with huge number of hits coming from collisions. The huge LHCb event rate leads to around 1 billion of particle tracks per second coming from pp collisions. Composed of 52 planes of silicon pixel sensors encircling the interaction region, the primary function is the reconstruction of Primary Vertices (PVs) and the generation of initial track seeds. These seeds are then propagated through the other detectors of the LHCb for further processing.

The reconstruction of straight-line tracks begins with the generation of three-hit seeds triplets from successive layers, using the algorithm called **Search by triplet** [50]. These triplets are then extended to other layers, considering that prompt particles from pp collisions that travel through the detector are straight lines with a constant polar ϕ angle from the PV. To facilitate rapid reference during the combination of hits into tracks, the hits on each layer are sorted by their ϕ angle. Lastly, these initial *VELO* tracks are refined using a simple Kalman filter [51].

3.8.2 *SciFi* track reconstruction

The *SciFi* track reconstruction is part of several algorithms inside the **Allen** framework, namely the **Forward** [49] and the **HybridSeeding** [52]. While the **Forward** algorithm is designed to reconstruct *long* tracks, **HybridSeeding** is able to reconstruct the standalone *SciFi* tracks.

3.8.3 *Long* track reconstruction

Two different algorithms are developed for *long* track reconstruction, named **Forward** and **Velo-SciFi Matching**. The first one relies on the extrapolation of *VELO* segments towards the SciFi plane, and sequential hit assignment afterwards. This does not require any standalone *SciFi* track segments. On the other hand, within the **Velo-SciFi Matching** algorithm, *VELO* tracks are matched to the *SciFi* track seeds reconstructed by the standalone seeding algorithm described above to create *long* tracks. This is shown in Fig. 12. The momentum kink depends on the integrated magnetic field along the path followed by the track and is calculated using MC simulations taking the magnetic field

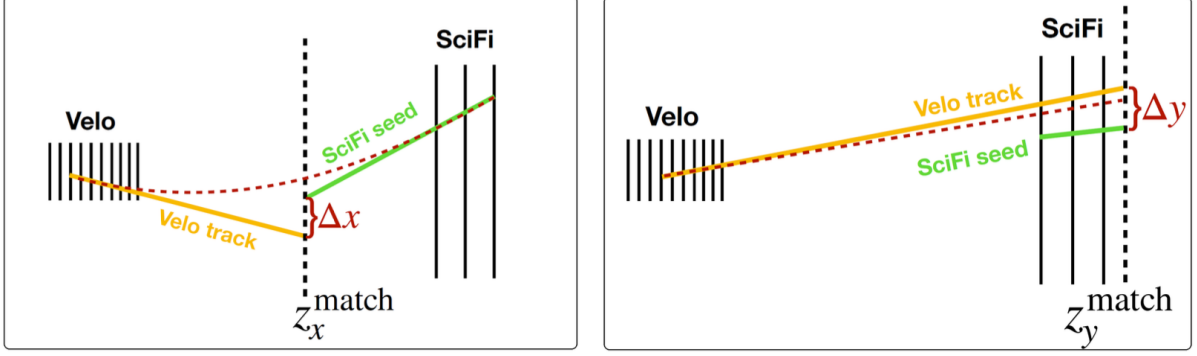


Figure 12: Illustration of the work principle of the **Matching** algorithm in the (left) $x - z$ plane and (right) $y - z$ plane [53].

map of LHCb detector into account. The ideal position to align the two track segments in a straight line model fluctuates basing on the momentum of the track. Hence, the z -position of the kink, termed z_x^{match} , is not static but rather includes the parameterisation of the magnetic field. Best candidates are selected using a χ^2 minimization strategy in Δx , Δy and Δt_y . Further, a clone-killing procedure is applied wherein the tracks that share a *VELO* track are compared and only the ones with the best χ^2 are kept.

The global averaged efficiency of **Velo-SciFi Matching** algorithm is greater than 80%, and for low momentum tracks is around 60%. The fake track rate is below 5% and the momentum resolution is below 1% for most of the tracks. The HLT1 throughput[‡] drop of this algorithm is only around 3% [7].

3.9 Downstream track reconstruction

3.9.1 Track reconstruction

The **Downstream** track reconstruction algorithm is based on the extrapolation of *SciFi* tracks to the UT detector through the LHCb dipole magnet. The extrapolation can be modeled as a sharp change in direction, akin to a *kink*, at a specific position along the z -axis. This position is termed as the “magnet point” and is denoted as z_{Magnet} . Using this point one can derive equations for x_{Magnet} and y_{Magnet} coordinate of the kink point:

$$\begin{aligned} z_{Magnet} &= \alpha_0 + \alpha_1 t_y^2 + \alpha_2 t_x^2 + \alpha_3 q/p + \alpha_4 |x_{SciFi}| + \alpha_5 |y_{SciFi}| + \alpha_6 |t_y| + \alpha_7 |t_x| \\ y_{Magnet} &= (y_{SciFi} + dy) + t_{y_{mag}}(z_{Magnet} - z_{SciFi}) \\ x_{Magnet} &= x_{SciFi} + t_x(z_{Magnet} - z_{SciFi}) \end{aligned} \quad (3.1)$$

Here, $t_x = \frac{dx}{dz}$, $t_y = \frac{dy}{dz}$, x_{SciFi} and y_{SciFi} are the slopes and coordinates of the track state in the last *SciFi* station, respectively. The initial signed track momentum estimate

[‡]It refers to the number of events the algorithm can process per time unit. It is a measure of the algorithm’s efficiency and performance under load.

is based on *SciFi* track parameters and is denoted as q/p . The coefficients $\alpha_0 - \alpha_7$ are determined using MC simulations.

Using the previous extrapolation, the search windows in each of the UT stations are defined in order to search for the corresponding hits. Once hit assigning process is done, the final track fit is performed [43].

Figure 13 shows an sketch of the algorithm strategy.

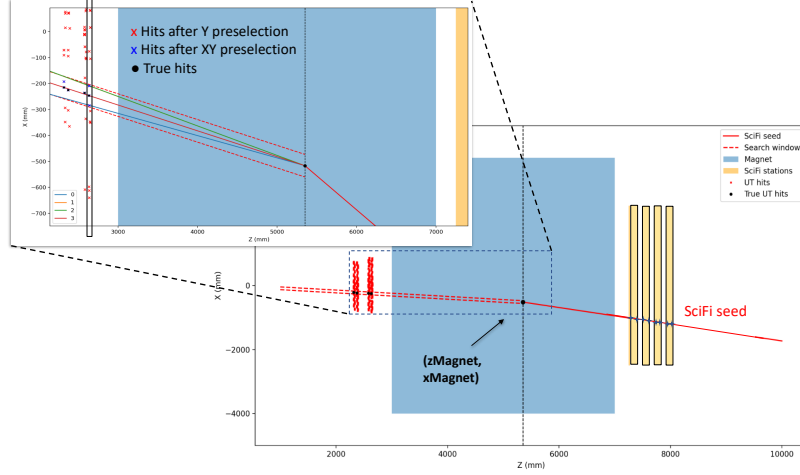


Figure 13: Strategy of the **Downstream** algorithm showing the used hits in the last UT layer and the Magnet Point (x_{Magnet} , z_{Magnet}) which is used to find the slope t_x . The slope is essentially the change in the x position of the particle with respect to the change in the z position from the Magnet Point to the UT stations.

3.9.2 Performance of the algorithm

The momentum resolution of *downstream* tracks is less than 2%. The global efficiency of the algorithm is about 80%. The ghost-tracks rate, due to tracks created from spurious hits from detector noise or imperfections, does not exceed 23% for most of the decay channels as shown at Fig. 14.

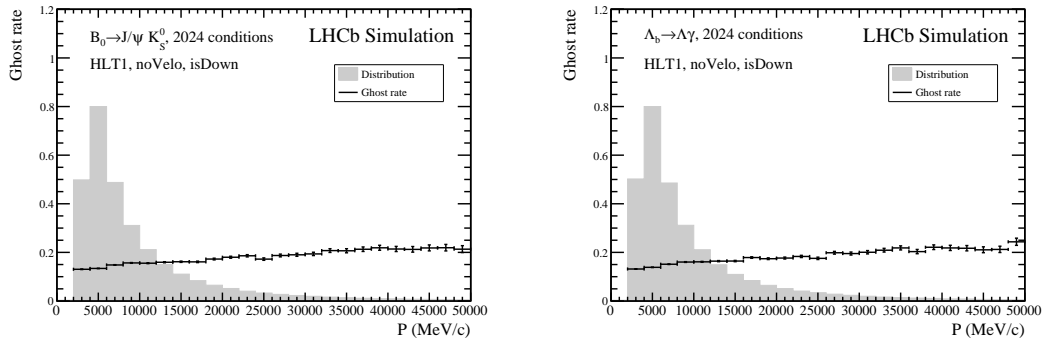


Figure 14: **Downstream** tracking ghost rate using $B_0 \rightarrow J/\psi K_S^0$ (left) and $\Lambda_b \rightarrow \Lambda^0 \gamma$ (right) simulated samples, as function of p . The gray distribution represents the normalized momentum distribution of all reconstructed tracks in the corresponding samples [43].

3.9.3 Physics efficiency

More than 75% of the *downstream* tracks are reconstructed by the algorithm in simulated samples. This has been verified for SM particles (Λ and K_S^0) from different physics decay channels as shown at Fig. 15.

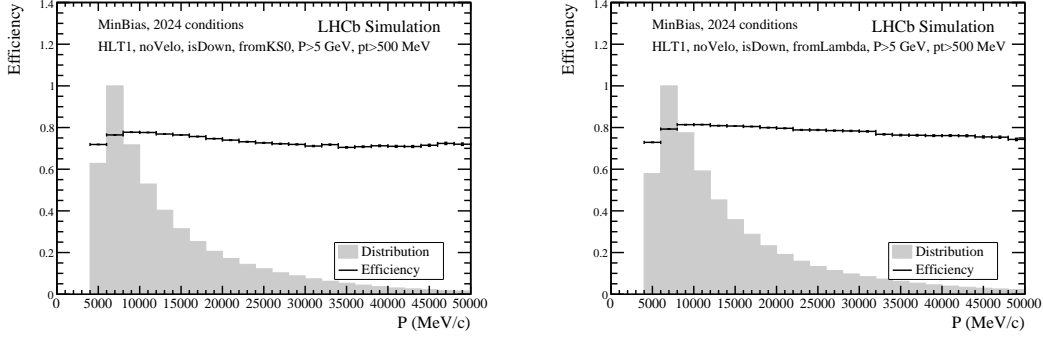


Figure 15: Efficiency of the **Downstream** algorithm as function of the momentum to reconstruct K_S^0 (top) and Λ (bottom) from minimum bias events. The gray distribution represents the normalized momentum distribution of all reconstructed tracks come from K_S^0 (top) and Λ (bottom) in this sample.[43]

The initial version of the tracking algorithm (Dv0) was developed with the primary goal of reconstructing tracks from Standard Model particles and was not optimized for the reconstruction of tracks from long-lived heavier particles. During the development of the **BuSca** project and the investigation of the potential application of the downstream tracking algorithm for the search for BSM particles, it was found that the reconstruction efficiency of the first version of the algorithm was relatively low. Consequently, a new version of the algorithm (Dv1) was developed, which is better adapted for the reconstruction of higher-mass particles, while maintaining high reconstruction efficiency for SM particles such as Λ and K_S^0 . Currently, the **downstream** reconstruction efficiency for particles with masses in the range of 2–5 GeV/ c^2 can vary between 50% and 80% before applying the ghost and clone killer[§] selection criteria, as shown in Fig. 16.

3.9.4 Downstream vertexing

The vertexing of two *downstream* tracks consists of reconstructing the secondary vertices with two *downstream* tracks using a Newton-Raphson method [54]. This technique is applied to find the point of closest approach between two extrapolated tracks, which is then used as the position of the secondary vertex. This method converges quickly, typically finding the solution in three iterations. The bias in the z and x positions of the vertex obtained using this technique are 14 cm and 1 cm, respectively. Figure 17 shows the improvement in the mass distributions for K_S^0 and Λ particles when applying vertex reconstruction to simulated samples.

[§]A dedicated algorithm to reduce duplicated track reconstruction due to ghost tracks.

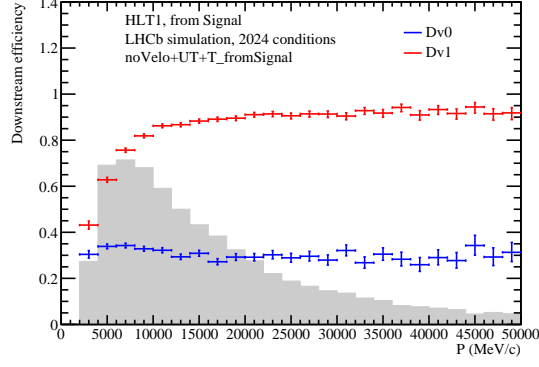


Figure 16: Efficiency comparison of the versions Dv0 and Dv1 of the **Downstream** algorithm for a new dark boson particle of mass $3 \text{ GeV}/c^2$ and lifetime of 2 ns. The gray distribution represents the normalized momentum distribution of all reconstructed signal tracks in the sample [43].

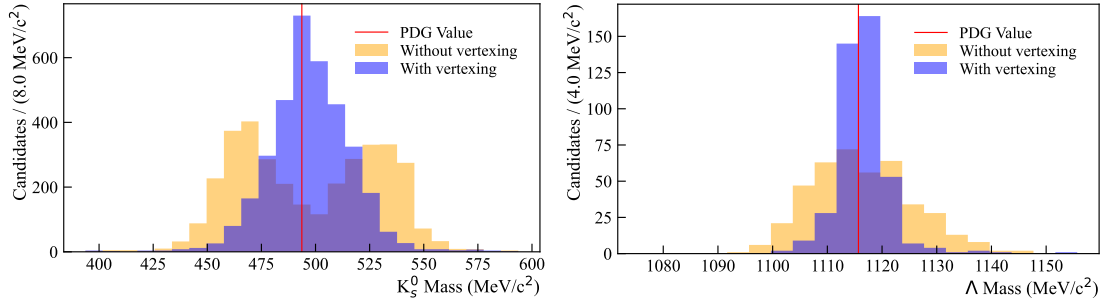


Figure 17: K_S^0 (left) and Λ (right) mass distributions before and after applying the vertex reconstruction as explained in the text. Values are compared with nominal (PDG) ones from the simulation. The mass resolution after applying the vertex reconstruction is 4 MeV and 15 MeV for K_S^0 and Λ decays respectively [43].

3.10 Studies of sensitivity to BSM particles

The impact of the **Downstream** algorithm on the LHCb physics performance is reported in [38]. After a detailed study including several models, the conclusion is that the **Downstream** setup hugely increases the LHCb physics possibilities towards the exploration of a diverse range of LLPs, competitive with the search potential of other LHC-based experiments like FASER2. A summary of this work is presented in the following.

3.10.1 BC4 and BC5 Scalar Boson Models

Models BC4 and BC5, which correspond to scalar bosons produced through different mechanisms, are of particular interest in this study. The BC4 scalar boson can be produced in processes such as $B \rightarrow SX$, where X is a hadronic state containing a quark and S is a hypothetical scalar boson. For a scalar mass M below the B meson mass and $\theta^2 \ll 1$, the total production rate is approximately $3.3\theta^2$. The allowed mass range for this scalar extends up to $5.13 \text{ GeV}/c^2$, corresponding to $M_B - M_\pi$. Figure 4 shows the normalized decay rate of this new scalar into different decay channels.

To explore the existence of these particles, the experimental search focuses on decays into two tracks that are stable within the LHCb detector. Therefore, we search for decays into $\pi\pi$, KK , or $\mu\mu$, which are the main channels in the mass range $0.27\text{--}2\text{ GeV}/c^2$, as shown in Fig. 18. For masses above $2\text{ GeV}/c^2$, decays are more likely to proceed through channels that involve hadronization, such as $c\bar{c}$, $s\bar{s}$, gg , or $\tau\tau$. In these cases, three or more tracks are expected to originate from a single displaced vertex.

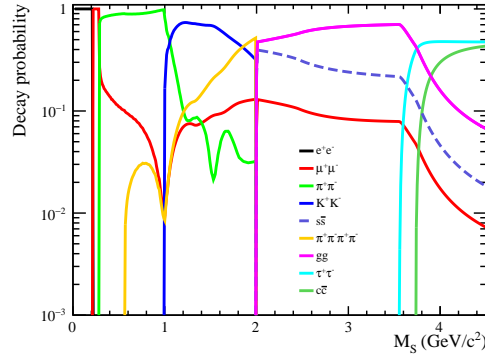


Figure 18: Decay probability of BC4 model into different channels [13].

A similar situation occurs for the BC5 model, which can be produced in the decay $H \rightarrow SS$. In this case, in addition to the mass regions already mentioned, the scalar boson can also have a mass between 5 and $60\text{ GeV}/c^2$. Most decays in this range are also expected to result in a hadronization process involving quarks and gluons; however, as with Standard Model bosons, there is still a possibility of decays into lepton pairs, although with a relatively small branching fraction.

The implementation of *downstream* tracks selections will enable us to explore up to two orders of magnitude in previously uncharted regions of parameter space for both models. The study, conducted in [38], highlights the potential of effectively utilizing the LHCb experiment by introducing the novel **Downstream** algorithm. This method allows for the investigation of events that do not produce hits in the VELO detector. Figure 19 illustrates the precise enhancement in sensitivity. The importance of the algorithm in terms of physics impact is outlined in the European Strategy for Particle Physics Update [55].

Compared to the current search strategies used by LHCb employing only long tracks, this algorithm provides several advantages: it allows triggering at the production vertex for the displaced vertex case, improves background suppression and increases the effective decay volume of the detector.

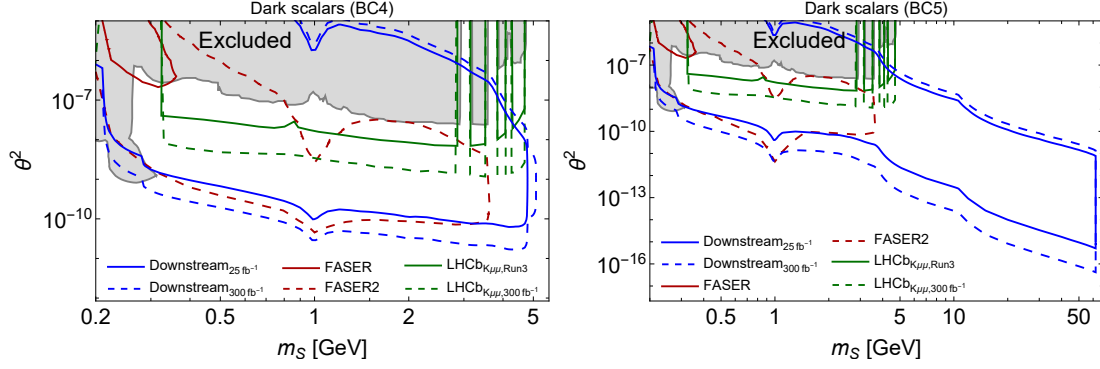


Figure 19: Sensitivity to Higgs-like scalars within model BC4 (the left plot) and BC5 (the right plot). [38]. The blue line represents the LHCb sensitivity region with the new **Downstream** reconstruction algorithm. The excluded parameter space is taken from [56, 57, 58].

4 BuSca framework

In addition to contributing to the development of the **Downstream** reconstruction algorithm and performing the sensitivities studies to BSM particles, the main work developed in this master thesis has been the development from scratch of the **BuSca** project framework to search for new particles in real time.

The trigger system implemented at LHCb on GPUs for Run 3 allows the possibility of developing new algorithms that access new phase space regions that have never been explored before. Since downstream reconstruction at the first level of the trigger was not possible during the Run 1 and Run 2 of LHCb, most of the events coming from long-lived particles decays were discarded at that time.

The **BuSca** framework opens a new strategy to search for long-lived BSM particles at LHCb. The idea is based on the reconstruction of two good-quality *downstream* tracks originated from a secondary vertex out of the VELO detector region. In addition to improve the reconstruction efficiency for long-lived SM particles like K_S^0 and Λ^0 , this idea can be extended and integrated into the existing reconstruction workflow to search for new particles. One of the main novelties introduced by the **BuSca** framework is the possibility of monitoring all reconstructed data without persisting them, and thus not affecting the trigger bandwidth, providing a tool to probe different parameter space regions.

BuSca does not depend on any specific BSM model, provided the BSM particle can decay into two tracks. This is accomplished through a specialized method for selecting vertices with good reconstruction quality, without relying on kinematic variables (further details will be provided later). Currently, **BuSca** operates exclusively with downstream tracks and vertices, focusing on decays into two tracks. Future expansions will include the study of jets with more tracks and the use of other types of tracks, thereby opening up even more phase space regions, still without requiring significant resources.

BuSca also provides a mechanism to ensure the proper reconstruction of objects and validate their quality, allowing comparisons of data and simulated events at the very initial

level of the selection chain. This, applied to specific mass regions with known SM particles, contributes to verify the proper operation of the detector, and to the understanding of background sources created from material interaction.

4.1 BSM particle simulations

Since **BuSca** is an algorithm that can detect any physics particle that decay into two charged particles, simulated samples with different possible BSM candidates were generated in this work and used, based on several theoretical models: ALP, Scalar Boson, and HNL [38]. Data transformation processes were necessary to process Monte Carlo (MC) samples within the HLT1 trigger level framework.

The execution chain proceeds as follows:

- Primary MC files are created using a Gauss [59] which combines Pythia8, Evtgen and Geant4, providing the generation of particles, their decays and the interaction with the detector, respectively.
- The LHCb detector response is modeled using Boole.
- Boole output is modified using Moore to simulate data storage for real data.

In this manner, samples are generated to accurately replicate the data achievable from the actual detector. In total, around 20M of events were generated with different geometrical conditions, physics models and geometrical cuts.

Configuration files for simulating the decays of a scalar boson, produced from b -hadron production, into muon-muon, pion-pion, and kaon-kaon pairs were developed during the project and added to the publicly accessible LHCb repository. These files were later used to simulate official Monte Carlo samples, each containing 1 million events. They are now available in the official library with identifiers: 12103045, 12103046, 12113069, 12113070 [60].

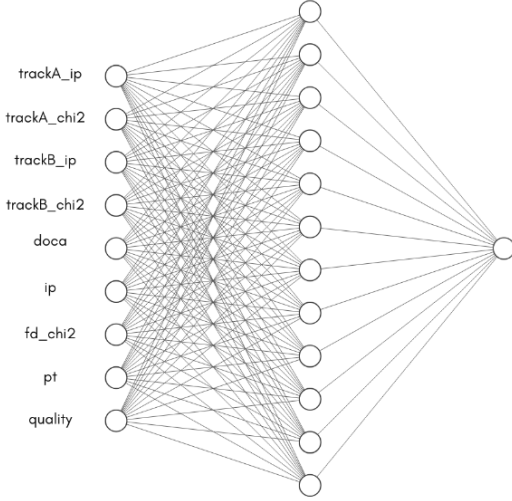
4.2 Selection

In order to select high-quality tracks in real time, a fast single-layer neural network (NN) is employed, which is trained using true SM pairs, such as K_S^0 , Λ and light resonances, though it can also be applied to the selection of any BSM model decaying into two tracks. Inputs to the NN, as shown in Fig. 20a, are parameters defining the track and vertex quality, in particular:

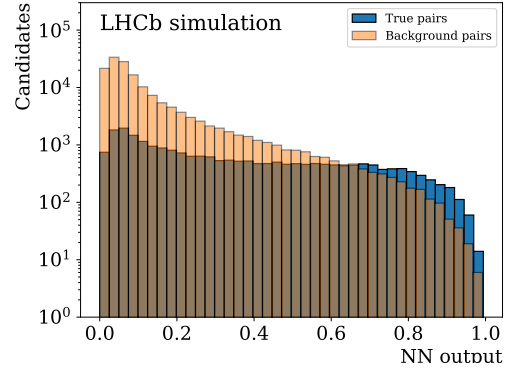
- Mother particle **impact parameter (IP)** - perpendicular distance between the path of a particle and the primary vertex (protons collision point).
- **DOCA** - **D**istance **O**f **C**losest **A**pproach between particle tracks.

- χ^2 the quality of the track or vertex reconstruction from the track or vertex fit. Usually this number is normalised by the number of degrees of freedom (ndf), and expressed as χ^2/ndf .
- **Track IP** - equivalent of the DOCA for a track and a vertex.
- χ^2_{FD} - the **F**light **D**istance (**FD**) significance of a decaying particle. Express the level of certainty on the FD measured from the primary vertex.

No kinematic information is used as inputs to the NN, as the aim is to remain as model-independent as possible. As output, a value between 0 and 1 is generated, as shown in Fig. 20b. Typically, a threshold is applied in the range of 0.5 to 0.9, depending on the desired level of track-quality selection tightness.



(a) BuSca NN architecture.



(b) Output of the NN for signal physics track-pairs and background track-pairs, the latter due mainly to fake tracks [61].

Figure 20: Neural network architecture (a) and performance (b) used in the BuSca project to select high-quality tracks at 30 MHz.

4.3 LHCb HLT1 monitoring system

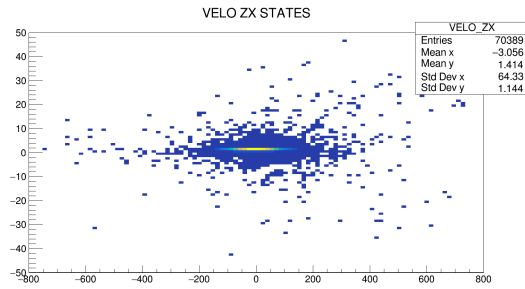
The LHCb Monitoring is utilized to investigate variables that may indicate the efficiency and accuracy of reconstruction and selection algorithms. A key feature of this monitoring at HLT1 stage is its minimal impact on trigger performance, allowing for the observation of a wide range of variables, such as the number of reconstructed tracks per event, the masses of reconstructed and selected pairs, and the number of hits in the detector. During the event processing, monitoring data is stored at the device (GPU), and approximately each second it is moved to the host (CPU). Such a design allows for running monitoring system in parallel.

The **BuSca** monitoring framework developed as part of this master thesis is designed to probe phase space regions which can give insights into new particle effects. The aim

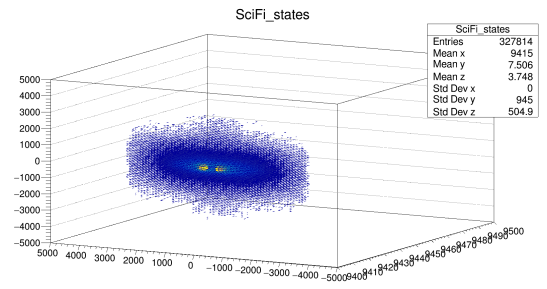
is recording the direct output from 30 MHz data rate in the form of 2D histograms. To be able to do that, the capability to utilize two-dimensional and three-dimensional histograms has been developed for HLT1, as previously only one-dimensional histograms were supported.

For each histogram, it is possible to configure each axis individually by adjusting the number of bins, as well as the minimum and maximum values. In addition, each axis can be assigned a variable scale, which may be advantageous for studying variables whose uncertainties depend on the value of the variable itself.

Figure 21 illustrates the application of two-dimensional and three-dimensional histograms within the HLT1 framework.



(a) A two-dimensional histogram of the distribution of hits in the VELO detector. The x -axis of the histogram corresponds to the z -axis of the detector, while the y -axis of the histogram corresponds to the x -axis of the detector.



(b) A three-dimensional histogram of hits in the SciFi detector. In this case, it is of particular interest to examine the distribution along all three axes: x , y , and z .

Figure 21: Examples of N-dimensions histograms inside HLT1.

4.4 BuSca histograms

The **BuSca** monitoring system is based on several two-dimensional histograms. These histograms are designed to efficiently store information about reconstructed vertices while minimizing memory usage. They are subsequently utilized in further analyses, such as the identification of regions with minimal background and the detection of potential signal peaks. The core functionality of **BuSca** involves two primary types of histograms: one that plots the reconstructed mass vs the flight distance of the parent particle, and the Armenteros–Podolanski distribution [62]. Additionally, for specific detector regions and mass ranges, a histogram of helicity versus mass is employed.

4.4.1 Mass versus Flight Distance

The mass versus flight distance histogram is filled with the assumption that the child particles are pions. This type of histogram facilitates the observation of peaks associated with displaced vertices. Figure 22 illustrates the pattern for a potential BSM particle with a mass of $2.5 \text{ GeV}/c^2$ and a lifetime of 400 ps. Additionally, the plot exhibits a populated

region or "hot line" on the left side, corresponding to reconstructed and selected K_S^0 and Λ^0 particles. This histogram can also be used to identify Standard Model light resonances produced inside the detector, as they will appear at well-known masses. The study of background and methods for its suppression will be discussed later in the 4.7 section.

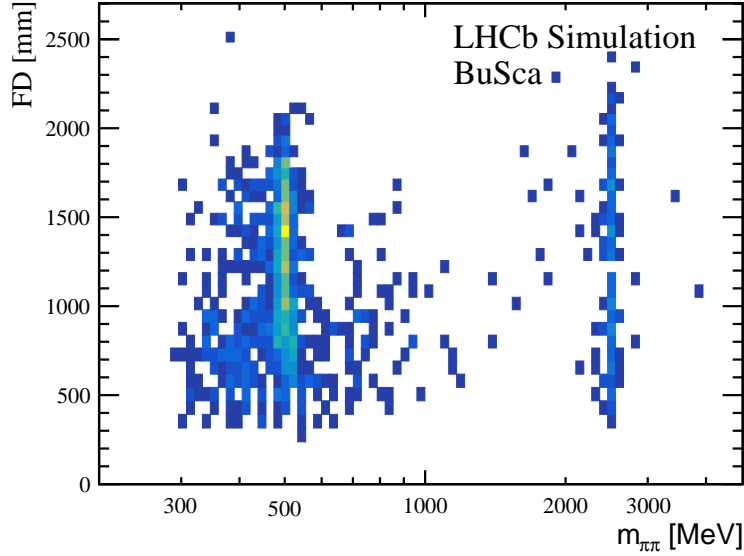
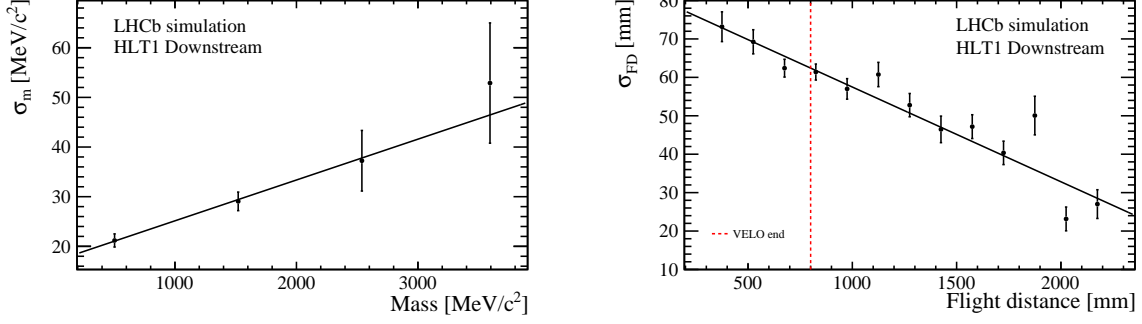


Figure 22: **BuSca** monitoring histograms: Mass versus flight distance. An event accumulation at low masses corresponding to K_S^0 candidates and other SM particles is observed. In the right part of the plot a clear excess corresponding to a new particle is evident [63]. The even generation of the new particle has been performed blindly, and checked to be properly reconstructed in the **BuSca** monitoring.

Given that the resolutions for mass and flight distance are dependent on their initial values, **BuSca** histograms are constructed using an adaptive binning approach, as illustrated in Fig. 22. Simulated Minimum Bias events, which are inelastic events selected with a trigger with as little bias as possible, are used for this evaluation. The reconstruction of the particle mass degrades for high masses since the track reconstruction algorithms are tuned using SM particles. The flight distance precision increases as the decay vertex approaches the UT detector. The parameterized resolution functions are displayed in the caption of Fig. 23.



(a) Mass resolution versus mass. The reconstruction of the particle mass degrades for high masses since the *downstream* track reconstruction and vertex algorithms are tuned using K_S^0 and Λ particles. The mass resolution is parameterised with a linear function: $\sigma_m = 0.02 \cdot m$ [MeV/c²] [61].

(b) Flight distance resolution vs flight distance. The closer the vertex is to the UT detector, the better the FD resolution due to the architecture of the **Downstream** reconstruction algorithm. The red line shows the end of the VELO detector. The parameterisation is $\sigma_{FD} = 80 - 0.02 \cdot FD$ [mm] [61].

Figure 23: Mass (a) and Flight distance (b) resolutions used to define the **BuSca** binning scheme [63]. Simulated Minimum Bias events are employed in this evaluation.

4.4.2 Armenteros-Podolanski plot

The Armenteros-Podolanski plot distribution is a representation of the sum of the child particles transverse momentum P_T of a two-body decay versus the asymmetry of the longitudinal momentum P_L of the decay products. In this plane, two-body decays appear as semi-ellipses, whose parameters provide information on the masses of the parent and the child particles. This representation was proposed in 1954 by R. Armenteros and J. Podolanski as a method of analysis of the dynamics of neutral particles decaying to two bodies (V_0 particles) [62]. It was used to separate $K_S^0 \rightarrow \pi^+\pi^-$ from $\Lambda^0 \rightarrow p\pi^-$ decays without any assumptions about the masses of the final state decay products. Conversely, by fitting the ellipses observed in data, one can retrieve the masses of the parent and the child particles. Deviations from known values then give useful information about detector and reconstruction effects, in particular biases in the momentum scale, which can be caused by, e.g., imperfect knowledge of the magnetic field of a detector [62].

The **Downstream** vertexing algorithm provides a slightly different variable for the y axis in the Armenteros-Podolanski plot, as compared to the standard one. In this modified version, the maximum of the ellipses, in case of symmetric decays (ex: $K_S^0 \rightarrow \pi^+\pi^-$), is linked to the mass of the parent particle. The exact formulas for calculations are:

$$p_i^L = (p_{ix} \cdot \mathbf{p}_x + p_{iy} \cdot \mathbf{p}_y + p_{iz} \cdot \mathbf{p}_z) / \mathbf{p}$$

$$p_{ix}^T = (p_{iy} \cdot \mathbf{p}_z - p_{iz} \cdot \mathbf{p}_y)$$

$$p_{iy}^T = (p_{iz} \cdot \mathbf{p}_x - p_{ix} \cdot \mathbf{p}_z)$$

$$p_{iz}^T = (p_{ix} \cdot \mathbf{p}_y - p_{iy} \cdot \mathbf{p}_x)$$

$$p_i^T = ((p_{ix}^T)^2 + (p_{iy}^T)^2 + (p_{iz}^T)^2) / \mathbf{p}$$

where \mathbf{p} - momentum of the parent particle in detector frame, p_i - momentum of child particle in detector frame.

An Armenteros-Podolanski example provided by **BuSca** is shown in Fig. 24 only with SM particles presented in the downstream region (such as K_S^0 and Λ^0). K_S^0 pairs create a big ellipse, with the center at (0; 0), while Λ^0 and $\bar{\Lambda}^0$ form two symmetric ellipses at left and right parts of the plot. The resulting ellipses are additionally highlighted with colored lines.

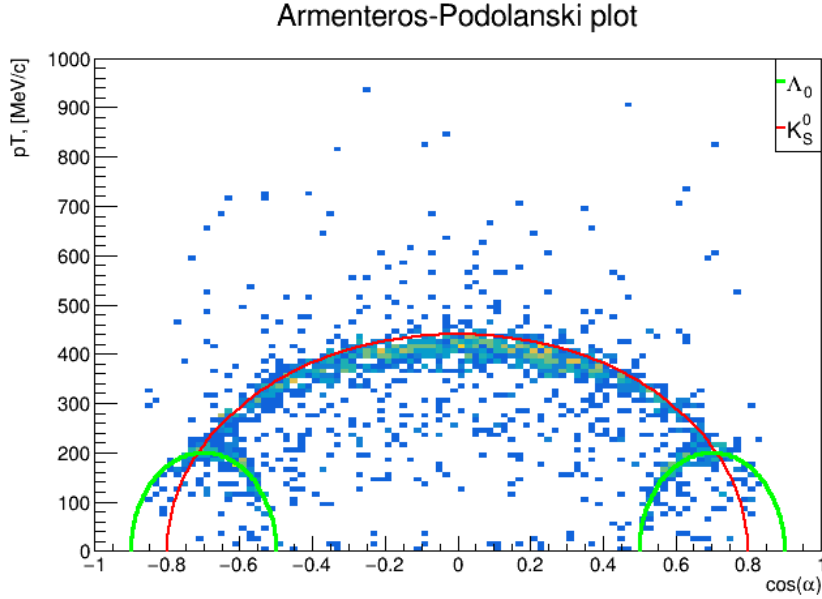


Figure 24: Armenteros-Podolanski plot with SM expectations

4.4.3 Helicity versus Mass histogram

In particle physics, helicity is the projection of a particle's spin onto the direction of its momentum. For practical purposes in vertex analyses, a simplified version of helicity is often used, especially for two-body decays.

The simplified helicity angle (θ^*) describes the angle between the momentum of a child particle (typically the positively charged one) in the parent's rest frame and the direction of the parent's momentum in the laboratory frame.

To compute θ^* , one has to first transform the child particle's momentum into the parent's rest frame, then find the angle between this momentum and the parent's momentum in the lab frame. The cosine of the helicity angle is given by:

$$\cos \theta^* = \frac{\vec{p}_{\text{child}}^* \cdot \vec{p}_{\text{parent}}}{|\vec{p}_{\text{child}}^*| |\vec{p}_{\text{parent}}|} \quad (4.1)$$

where

\vec{p}_{child}^* is the momentum of the child particle in the parent's rest frame,

\vec{p}_{parent} is the momentum of the parent particle in the laboratory frame.

The helicity angle is particularly valuable in distinguishing between different SM or BSM decay processes. For example, in the decay of a vector meson such as the J/ψ into two leptons, the distribution of the helicity angle is expected to follow a characteristic $\sin^2(\theta^*)$ shape, reflecting the spin-1 nature of the parent particle. In contrast, for the decay of a pseudoscalar meson such as the B^0 into two spinless particles, the helicity angle distribution is expected to be flat, as there is no preferred direction for the emission of the child particles. By comparing the observed helicity angle distributions to these theoretical expectations, one can effectively identify the spin and parity of the parent particle, discriminating between signal and background processes, and test for possible contributions from new physics beyond the Standard Model. More examples of helicity distribution of SM decays can be seen in Fig. 25.

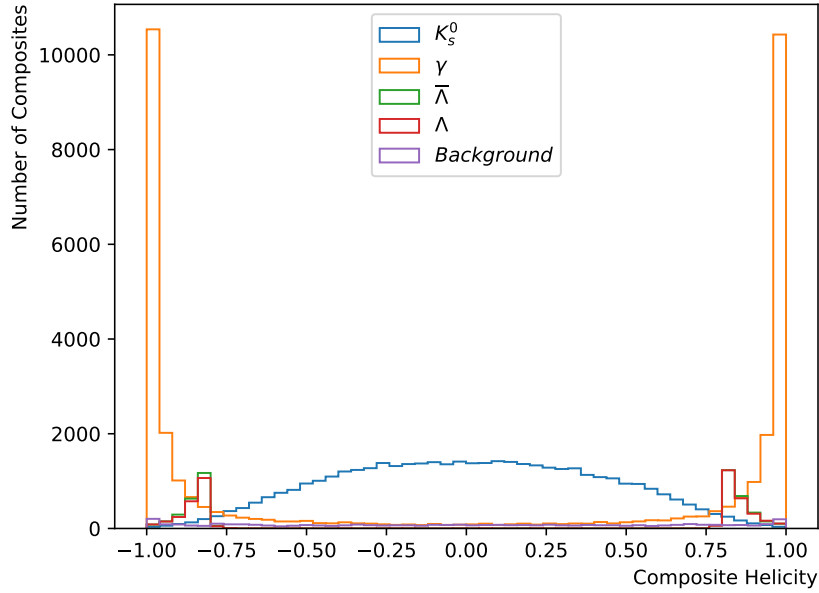


Figure 25: Helicity distribution for SM decays.

4.4.4 High Mass monitoring

In addition to the mass versus flight distance histogram in a typical low-mass range below $5 \text{ GeV}/c^2$, experimental monitoring histograms are also kept for vertices with reconstructed masses in the range of $5\text{--}50 \text{ GeV}/c^2$. A notable characteristic of this region is the absence of expected Standard Model particles in the downstream region, as all Standard Model resonances decay within the VELO detector and lack the requisite lifetime to traverse a distance of 1 meter. This will be further explained in the following sections.

Moreover, interactions of particles with the detector material do not yield particles with masses within this range. Consequently, in this region, no contribution from genuine physical pairs is anticipated, with only very few combinatorial background expected, which will be examined in detail in subsequent analyses.

4.5 BuSca selection lines

In addition to its monitoring capabilities, **BuSca** incorporates trigger lines for both HLT1 and HLT2 stages. These trigger lines are designed to facilitate the study of events deemed interesting at the offline level, particularly in the context of jet reconstruction. Implementation occurs at both trigger levels, with the primary selection executed at the HLT1 stage, employing the aforementioned selection criteria. Additional constraints are imposed to exclude Standard Model particles such as K_S^0 and Λ^0 . The threshold for the neural network output is deliberately set low to mitigate the impact of imperfect reconstruction or potential inefficiencies in selection processes. Currently, this threshold is established at 0.2, with the possibility of adjustment in future studies contingent upon available bandwidth.

Presently, three principal lines are utilized for data acquisition: the hadron-hadron line, which focuses on reconstructing and selecting pairs, primarily $\pi\pi$ and KK . Given the prevalence of such pairs in events, this line is postscaled with a rate of 0.01 to adhere to trigger bandwidth limitations. The muon-muon and electron-electron lines, employed for the reconstruction of leptonic pairs, apply identical constraints to reduce the incidence of Standard Model pairs but do not employ a prescale rate, as the overall number of such pairs is comparatively limited.

At the HLT2 stage, **BuSca** refrains from imposing additional selection criteria to ensure that the reconstructed pairs are physically significant and not merely background artifacts. Consequently, the selection of pairs relies exclusively on the HLT1 selection, thereby minimizing dependence on the HLT2 level.

4.6 BuSca performance impact

The impact of the **BuSca** algorithm during the online data-taking period can be assessed by examining the throughput and trigger bandwidth. These metrics account for data histogramming, neural network selection, vertex reconstruction, and the selection of trigger lines. The observed effects are minimal, with less than a 0.5% increase in throughput and less than a 0.1% increase in trigger bandwidth. These values are measured using real data collected in October 2024, during which the **BuSca** algorithms were active, and are consistent with expectations from simulation, as shown in Fig. 26.

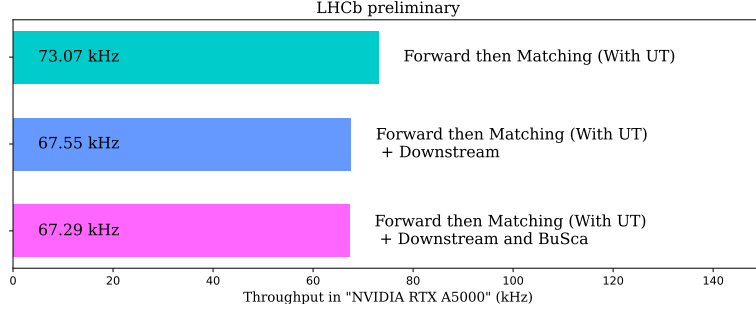


Figure 26: Throughput of the Allen sequence, without and including the **Downstream** algorithm, executed on a RTA A5000 card using data from October 2024, Run 306411 [61]. **Forward then Matching** algorithm is used for the reconstruction of *long* tracks. The global effect of the inclusion of **BuSca** in the rate is 0.26 kHz.

4.7 Background studies

One of the most important conditions for searches of new particles is to reduce the background to a negligible level, to avoid that it is misidentified as a signal candidate. The downstream region offers a cleaner region as compared to analysis performed with *long* tracks, but still possible background contributions need to be studied. In this work possible background sources have been separated in three categories: hadronic resonances, created at the interaction point or by material interaction; strange candidates from SM such as K_S^0 and Λ ; and combinatorial background, originated by random combinations of tracks.

Two tracks with the same charge, named same-sign candidates, are not expected to originate from physics processes and do not create a mass peak in the **BuSca** histograms. Since parallel to opposite-sign data, histograms in **BuSca** are filled with these same-sign candidates, detailed studies are performed using both simulated and real data events. They are detailed in the following.

4.7.1 Hadronic resonances

Hadronic resonances that decay into either two leptons or two hadrons (primarily pions) may originate from proton-proton collisions or from particle interactions with the beam pipe and detector materials, thereby mimicking a signature characteristic of beyond the Standard Model signals. In the case of prompt resonances produced directly in proton-proton collisions, their extremely short lifetimes result in decays occurring within the VELO detector, and thus they do not contribute to the background in the downstream region, which extends longitudinally from 800 mm to 2500 mm.

However, such resonances can become relevant if they are produced via material interactions (MI). To identify and study these cases, a material map of the downstream region has been constructed, as illustrated in Fig. 27.

Figure 27 displays vertices arising from material interactions, as obtained from simulated minimum bias events. The beam pipe and various detector layers are clearly visible in this representation. For the purpose of background characterization, the detector has been divided into six distinct flight distance (FD) regions, each with a width of 400 mm. The first two regions (D1–D2) correspond to the VELO area, where a substantial amount of material is present. The remaining regions are primarily populated by interactions with the beam pipe and other mechanical components. The final region (D6) is predominantly influenced by material interactions with the UT detector.

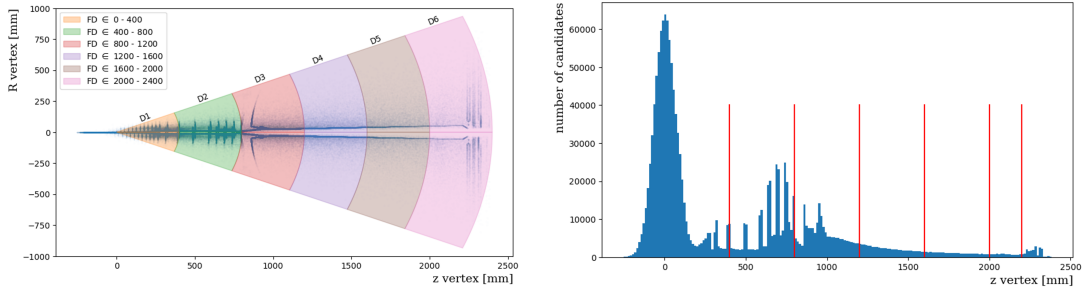


Figure 27: Material map obtained from downstream vertices in simulated minimum bias events. The beam pipe and detector structure can be clearly seen (top). Six different regions are defined D1–D6 and shown with different colours. The projection of number of vertices is also shown with red lines indicated the region boundaries (bottom) [61].

According to the Minimum Bias simulation, particles with masses below $2 \text{ GeV}/c^2$, such as K_S , K_L , Λ^0 , ρ , η , and η' are produced in detector regions predominantly by MI. Additionally, γ conversions into e^+e^- pairs are also found in simulation. With the recent inclusion of new states decaying into two hadrons in the Pythia event generator, based on the latest experimental results [64], an investigation of additional possible contributions has been conducted. This study specifically considers resonances such as $f_0(500)$, $f_0(980)$, f_2 , and $\rho^0(1700)$.

No resonances originating from material interactions are observed at masses above $3 \text{ GeV}/c^2$, and this conservative threshold has been adopted for regions where MI is dominant. For the region between 1.2 m. and 2.0 m., this threshold can be relaxed to $2 \text{ GeV}/c^2$, as confirmed by both same-sign and opposite-sign data. Mass spectrum from these regions are shown in Fig. 28. Such mass cut is used even when analyzing di-muon channels, as misidentified pions from material interactions may otherwise contribute to background in this channel.

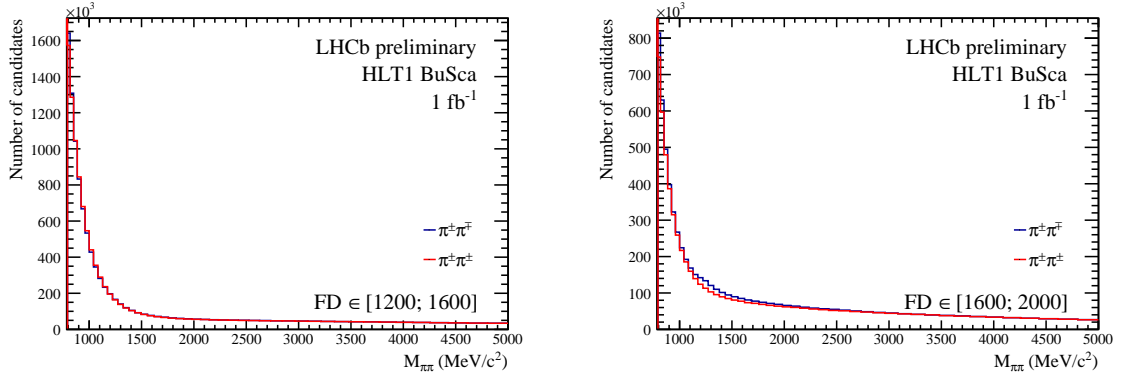


Figure 28: Mass projection of the monitoring 2D BuSca plot for opposite sign (blue) and same sign (red) tracks. The latter is expected to originate from combinatorial pairs. A mass larger than $800 \text{ MeV}/c^2$ is required to suppress the contribution of K_S^0 decays into two pions for opposite-sign candidates. A FD selection criteria of 1.2-1.6 m (left) and 1.6-2.0 m (right) are also imposed..

4.7.2 Strange candidates

Strange candidates from the SM, decaying into two particles, such as K_S^0 and Λ particles, populate the downstream region. To avoid their contribution, a veto can be applied in the mass region associated with these candidates. In Fig. 29, $K_S^0 \rightarrow \pi^+\pi^-$ and $\Lambda \rightarrow p\pi^-$ downstream candidates are shown from real data.

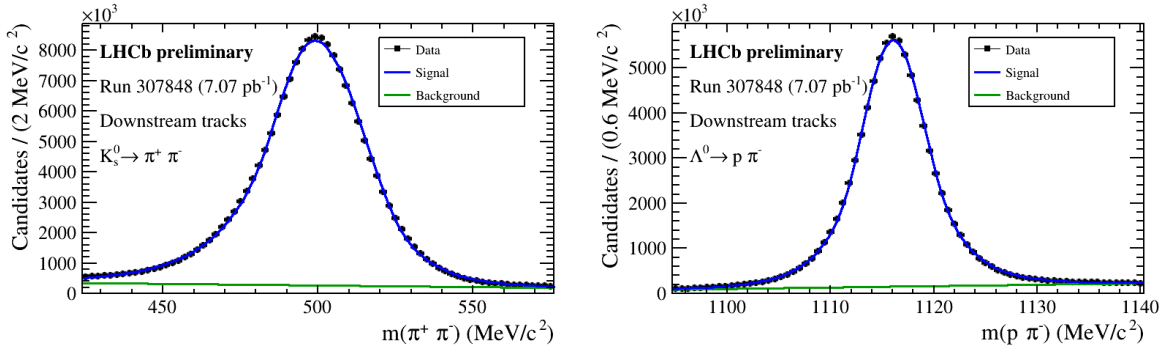


Figure 29: Mass distributions of $K_S^0 \rightarrow \pi^+\pi^-$ decays (left) and $\Lambda \rightarrow p\pi^-$ decays (right) reconstructed by the **Downstream** algorithm, corresponding to an integrated luminosity of 7.07 pb^{-1} . The mass resolution is $15 \text{ MeV}/c^2$ and $3 \text{ MeV}/c^2$ for K_S^0 and Λ , respectively [65].

Inspecting simulated samples, no K_S^0 or Λ candidates are observed at masses larger than $1.5 \text{ GeV}/c^2$, when they are reconstructed using the pion mass hypothesis for the decay particles. This conservative veto is applied to avoid background contributions from strange candidates.

4.7.3 Combinatorial background

Combinatorial background arises from random combinations of two high-quality tracks. To address this source of background, two tracks with the same sign are paired, and a fake vertex is reconstructed. These same-sign (SS) candidates are expected to have the same

behavior as the random combinations of opposite-sign (OS) candidates. In Fig. 30, the **BuSca** mass projection for SS and OS candidates from simulated events, assuming the pion mass hypothesis, is shown. At low mass (≤ 700 MeV/c²), contributions from strange signals such as K_S^0 , Λ and photon candidates converted in e^+e^- pairs, are observed for OS candidates.

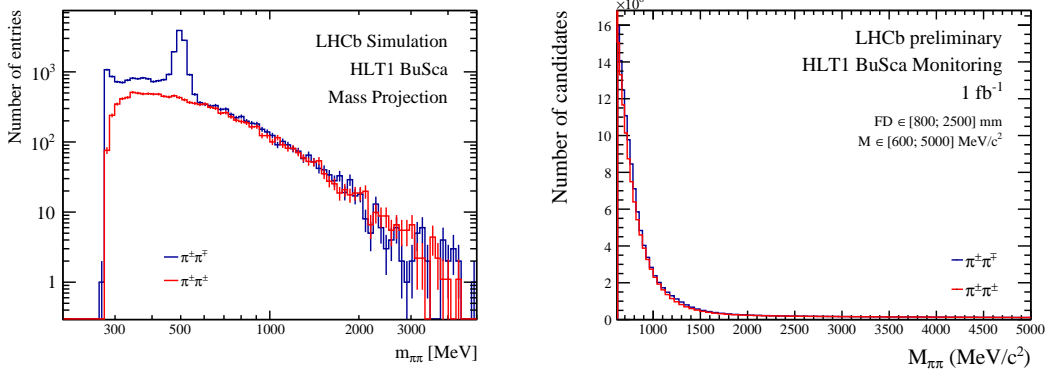


Figure 30: Mass distribution of SS and OS two-track candidates, from simulated events (left) [61] and 1 fb⁻¹ of real data (right) [66], assuming di-pion mass, selected with the **BuSca** track-quality neural network in the monitoring block. No normalization condition is applied in these distributions.

The combinatorial background component, evident for masses above 600 MeV/c², is well described by fake vertices originating from SS candidates. Since high-momentum tracks are relatively rare, the number of vertices formed from random combinations decreases sharply with increasing mass. As it can be observed in these figures, SS combinations properly describe the combinatorial background. Functional shapes can be obtained from SS data using the **BuSca** monitoring system to determine a threshold for searches in real time.

In order to further suppress this background, dedicated AI techniques are being investigated to be applied in the **BuSca** framework. In particular, an autoencoder trained with SS candidates from real data is planned to be used for combinatorial background suppression and anomaly detection.

4.8 BuSca results using 2024 data

During a two-week period in October 2024, the **BuSca** project was deployed and tested in the online data-taking, corresponding to 1 fb⁻¹ integrated luminosity. The first results are shown in Fig. 31. Pairs are selected with tight criteria for the NN track quality. In Fig. 31 (left) the **BuSca** mass distribution is shown with a clear excess from K_S^0 and Λ particles at the low mass region. In the same figure (right) the Armenteros-Podolanski distribution is shown. At the bottom of the figure, K_S^0 pairs from pp interactions create a big ellipse, with center at (0, 0), while Λ and $\bar{\Lambda}$ candidates from pp interactions form two symmetric

ellipses at the left and right bottom of the plot. A small accumulation due to converted photons can also be observed in the central region at low transverse momentum.

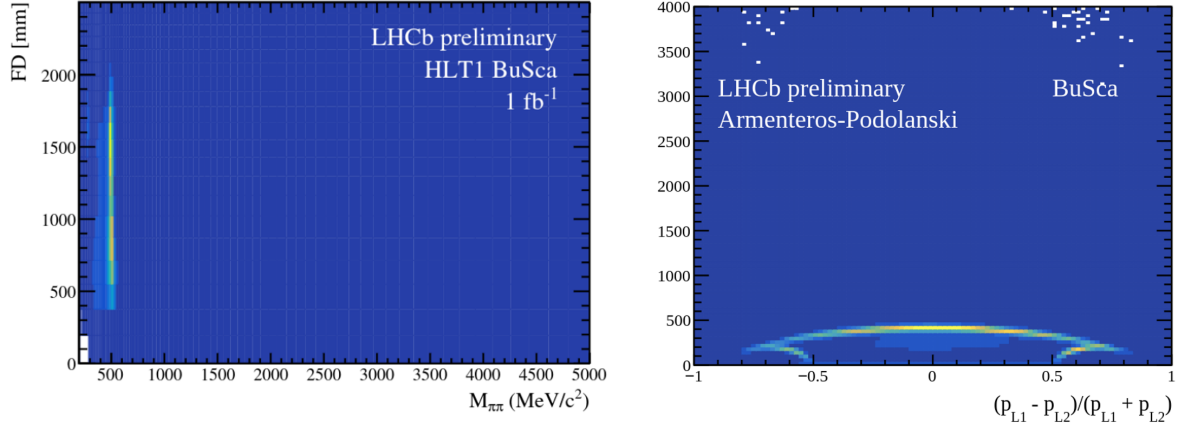


Figure 31: First data results from the **BuSca** project, acquired during a commissioning two-week period in October 2024. The **BuSca** mass distribution (left) shows a clear excess from K_S^0 and Λ particles at the low mass region. The Armenteros-Podolanski distribution (right) also shows ellipses for K_S^0 , and Λ and $\bar{\Lambda}$ candidates [63].

4.9 Application for detecting incorrect reconstruction

During the analysis of data collected by **BuSca** in October 2024, an anomaly was identified in the reconstruction of downstream pairs at the HLT2 level. In the examination of pairs reconstructed with a vertex Z greater than 2000 mm, a peak with a mass of 2.6 GeV/c^2 was observed, which does not correspond to any particle from the Standard Model. An investigation of the same region at the HLT1 level revealed no such a peak. Figure 32 illustrates the mass distribution found at HLT2 level. The mass peak is fitted using a Crystal-Ball function [67], employed for fitting the mass spectrum of most Standard Model resonances since it includes a mean value for the mass and asymmetric widths, is shown in the right part of the plot.

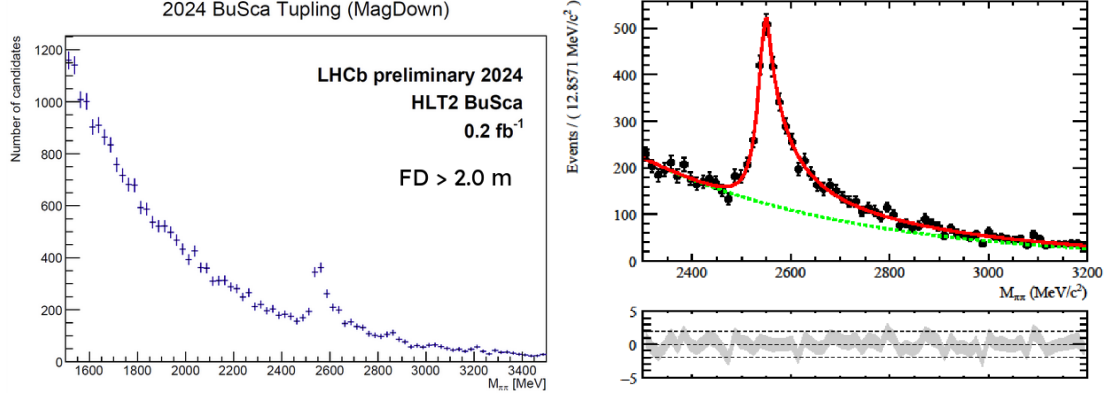


Figure 32: HLT2 mass distribution (left) and fit to the mass peak using a Crystal-Ball distribution (right). The fit results are 2768 events in the peak (no PV constraint), $M = 2.552(1) \text{ GeV}/c^2$, $\sigma_R = 18 \text{ MeV}/c^2$, $\sigma_L = 9 \text{ MeV}/c^2$.

Further investigations of the peak revealed that it is a result of an incorrect pair reconstruction from HLT2 algorithms for cases where reconstruction occurs with $Z > 2500 \text{ mm}$. For HLT1, such an anomaly was not observed due to an imposed vertex constraint of $Z < 2500 \text{ mm}$. The data behavior is also observed in simulated samples, which indicate that nearly all pairs that compose the peak are combinatorial background and the effect comes from a reconstruction artifact. indeed, it was observed that for high-momentum very-collimated tracks, they deviate in the point of maximum magnetic field (around 5.5 m) creating a fake vertex. These fake candidates can be removed avoiding regions downstream the UT detector, or further improve HLT2 algorithms to avoid this happens.

4.10 Prospects

BuSca will continue to be used until the end of Run 3, with potential further improvements that may enable the exploration of additional physics models. One example currently under development is the use of the *corrected mass* variable, which is particularly relevant for studying decays involving neutrinos that cannot be directly detected. In such cases, energy and momentum are lost, making it impossible to reconstruct the decay vertex using only two tracks; instead, the mass must be corrected based on the momenta of the visible particles.

Another ongoing effort is the implementation of an anomaly detection neural network, or autoencoder, which will be trained exclusively on same-sign track pairs from real data. This approach allows the network to learn from combinatorial backgrounds and material interaction pairs, using only real data for training, with subsequent validation performed on Monte Carlo simulations.

During the technical stop scheduled between 2026 and 2030, there are plans to add support for vertices containing T tracks, thereby enabling the reconstruction of particles with even longer lifetimes. Additionally, the possibility of reconstructing jets composed

of three or more tracks directly at the HLT1 level is being considered, although this will likely require significant computational resources.

The data collected during the present year will be analyzed with **BuSca** providing signal insights or exclusion limits for several BSM models.

5 Conclusions

The new trigger scheme of the LHCb experiment offers a promising approach for BSM searches, particularly for long-lived particles. The **Downstream** tracking and vertexing techniques developed and introduced during Run 3 have provided access to a previously unexplored region, allowing for the search for long-lived particles. A new project called BuSca (Buffer Scanner) is introduced, with a pioneering model-independent search algorithm at the first high-level trigger of LHCb, executed at a rate of 30 MHz. It reconstructs secondary vertices from high-quality, very-displaced tracks and selects good signal candidates by using a fast neural network. This algorithm, which has access to the full online data, is already in use, and its performance has been studied with 1 fb^{-1} data from October 2024. In 2025, an additional 2.5 fb^{-1} of data was collected by **BuSca**, and the collection will continue.

Currently, **BuSca** is already being utilized to study various types of background that may affect future searches for particles beyond the Standard Model: the study of light resonances formed as a result of interactions of passing particles through the detector, research into methods for reducing the impact of long-lived Standard Model particles, such as K_S^0 and Λ . Evaluation of methods to suppress combinatorial background using modern machine learning techniques, as well as strategies for choosing the best phase space regions for searches.

This work is pioneer and has developed from scratch for this master thesis. It has been presented in two international conferences: CHEP24 (Conference on Computing in High Energy and Nuclear, Krakow) and LLP25, (15th Workshop of the Long-Lived Particles, Valencia). The work also will be presented at EPS25 (European Physical Society Conference on High Energy Physics, Marseille).

References

- [1] A. Arbuzov, “Quantum field theory and the electroweak standard model,”.
- [2] A. Collaboration *et al.*, “Observation of a new particle in the search for the Standard Model Higgs boson with the ATLAS detector at the LHC,” *arXiv preprint arXiv:1207.7214* (2012) .
- [3] C. Collaboration *et al.*, “Observation of a new boson at a mass of 125 GeV with the CMS experiment at the LHC,” *arXiv preprint arXiv:1207.7235* (2012) .
- [4] M. E. Peskin, *An introduction to quantum field theory*. CRC press, 2018.
- [5] P. W. Higgs, “Broken symmetries and the masses of gauge bosons,” *Physical review letters* **13** no. 16, (1964) 508.
- [6] F. Englert and R. Brout, “Broken symmetry and the mass of gauge vector mesons,” *Physical review letters* **13** no. 9, (1964) 321.
- [7] B. K. Jashal, “Triggering new discoveries: development of advanced HLT1 algorithms for detection of long-lived particles at LHCb.” 2023.
<https://cds.cern.ch/record/2881886>. Presented 07 Nov 2023.
- [8] L. Lee, C. Ohm, A. Soffer, and T.-T. Yu, “Collider searches for long-lived particles beyond the Standard Model,” *Progress in Particle and Nuclear Physics* **106** (2019) 210–255.
- [9] R. Allahverdi, N. P. D. Loc, and J. K. Osiński, “Dark matter and baryogenesis from visible-sector long-lived particles,” *Physical Review D* **107** no. 12, (June, 2023) .
<http://dx.doi.org/10.1103/PhysRevD.107.123510>.
- [10] J. Beacham *et al.*, “Physics Beyond Colliders at CERN: Beyond the Standard Model Working Group Report,” *J. Phys. G* **47** no. 1, (2020) 010501,
[arXiv:1901.09966](https://arxiv.org/abs/1901.09966) [hep-ex].
- [11] **SHiP** Collaboration, C. Ahdida *et al.*, “Sensitivity of the SHiP experiment to dark photons decaying to a pair of charged particles,” *Eur. Phys. J. C* **81** no. 5, (2021) 451, [arXiv:2011.05115](https://arxiv.org/abs/2011.05115) [hep-ex].
- [12] P. Ilten, Y. Soreq, M. Williams, and W. Xue, “Serendipity in dark photon searches,” *JHEP* **06** (2018) 004, [arXiv:1801.04847](https://arxiv.org/abs/1801.04847) [hep-ph].
- [13] I. Boiarska, K. Bondarenko, A. Boyarsky, V. Gorkavenko, M. Ovchinnikov, and A. Sokolenko, “Phenomenology of GeV-scale scalar portal,” *JHEP* **11** (2019) 162, [arXiv:1904.10447](https://arxiv.org/abs/1904.10447) [hep-ph].

- [14] C. Antel *et al.*, “Feebly Interacting Particles: FIPs 2022 workshop report,” in *Workshop on Feebly-Interacting Particles*. 5, 2023. [arXiv:2305.01715](#) [hep-ph].
- [15] K. Bondarenko, A. Boyarsky, D. Gorbunov, and O. Ruchayskiy, “Phenomenology of GeV-scale Heavy Neutral Leptons,” *JHEP* **11** (2018) 032, [arXiv:1805.08567](#) [hep-ph].
- [16] G. Dalla Valle Garcia, F. Kahlhoefer, M. Ovchinnikov, and A. Zaporozhchenko, “Phenomenology of axion-like particles with universal fermion couplings – revisited,” [arXiv:2310.03524](#) [hep-ph].
- [17] D. Aloni, Y. Soreq, and M. Williams, “Coupling QCD-Scale Axionlike Particles to Gluons,” *Phys. Rev. Lett.* **123** no. 3, (2019) 031803, [arXiv:1811.03474](#) [hep-ph].
- [18] M. Ovchinnikov, J.-L. Tastet, O. Mikulenko, and K. Bondarenko, “Sensitivities to feebly interacting particles: public and unified calculations,” *Phys. Rev. D* **108** no. 7, (5, 2023) 075028, [arXiv:2305.13383](#) [hep-ph].
- [19] CERN, “Project schedule,” <https://project-hl-lhc-industry.web.cern.ch/content/project-schedule>. Accessed: [30/06/2025].
- [20] A. Team, “The four main LHC experiments,” 1999.
- [21] R. Aaij, B. Adeva, *et al.*, “Search for massive long-lived particles decaying semileptonically in the LHCb detector,” *The European Physical Journal C* **77** (2017) 1–16.
- [22] R. Aaij, B. Adeva, *et al.*, “Updated search for long-lived particles decaying to jet pairs,” *The European Physical Journal C* **77** (2017) 1–14.
- [23] R. Aaij, B. Adeva, *et al.*, “Search for Higgs-like bosons decaying into long-lived exotic particles,” *The European Physical Journal C* **76** (2016) 1–15.
- [24] **LHCb** Collaboration, R. Aaij *et al.*, “Search for Majorana neutrinos in $B^- \rightarrow \pi^+ \mu^- \mu^-$ decays,” *Phys. Rev. Lett.* **112** no. 13, (2014) 131802, [arXiv:1401.5361](#) [hep-ex].
- [25] R. Aaij, C. Abellan Beteta, *et al.*, “Searches for Majorana neutrinos in B-decays,” *Physical Review D—Particles, Fields, Gravitation, and Cosmology* **85** no. 11, (2012) 112004.
- [26] R. Aaij, B. Adeva, *et al.*, “Search for hidden-sector bosons in $B^0 \rightarrow K^{*0} \mu^+ \mu^-$ decays,” *Physical review letters* **115** no. 16, (2015) 161802.

- [27] **LHCb** Collaboration, R. Aaij *et al.*, “Search for long-lived scalar particles in $B^+ \rightarrow K^+ \chi(\mu^+ \mu^-)$ decays,” *Phys. Rev. D* **95** no. 7, (2017) 071101, [arXiv:1612.07818 \[hep-ex\]](#).
- [28] R. Aaij, B. Adeva, *et al.*, “Search for long-lived heavy charged particles using a ring imaging Cherenkov technique at LHCb,” *The European Physical Journal C* **75** (2015) 1–14.
- [29] **LHCb** Collaboration, R. Aaij *et al.*, “Search for $A' \rightarrow \mu^+ \mu^-$ Decays,” *Phys. Rev. Lett.* **124** no. 4, (2020) 041801, [arXiv:1910.06926 \[hep-ex\]](#).
- [30] **MoEDAL-MAPP** Collaboration, B. Acharya *et al.*, “MoEDAL-MAPP, an LHC Dedicated Detector Search Facility,” in *Snowmass 2021*. 9, 2022. [arXiv:2209.03988 \[hep-ph\]](#).
- [31] D. Curtin, M. Drewes, *et al.*, “Long-lived particles at the energy frontier: the MATHUSLA physics case,” *Reports on progress in physics* **82** no. 11, (2019) 116201.
- [32] G. Aielli *et al.*, “The Road Ahead for CODEX-b,” [arXiv:2203.07316 \[hep-ex\]](#).
- [33] J. L. Feng, I. Galon, F. Kling, and S. Trojanowski, “ForwArd Search ExpeRiment at the LHC,” *Phys. Rev. D* **97** (Feb, 2018) 035001. <https://link.aps.org/doi/10.1103/PhysRevD.97.035001>.
- [34] S. Collaboration, “The SHiP experiment at the proposed CERN SPS Beam Dump Facility.” 2022. <https://arxiv.org/abs/2112.01487>.
- [35] J. Alimena *et al.*, “Searching for long-lived particles beyond the Standard Model at the Large Hadron Collider,” *J. Phys. G* **47** no. 9, (2020) 090501, [arXiv:1903.04497 \[hep-ex\]](#).
- [36] L. Henry, B. Jashal, V. Kholoimov, D. Mendoza, A. Oyanguren, V. Svintozelskyi, and J. Zhuo, “Impact of the high-level trigger for detecting long-lived particles at LHCb,” *EPJ Web Conf.* **295** (2024) 02015.
- [37] **LHCb** Collaboration, R. Aaij *et al.*, “The LHCb upgrade I,” [arXiv:2305.10515 \[hep-ex\]](#).
- [38] V. Gorkavenko, B. K. Jashal, V. Kholoimov, Y. Kyselov, D. Mendoza, M. Ovchynnikov, A. Oyanguren, V. Svintozelskyi, and J. Zhuo, “Lhcb potential to discover long-lived new physics particles with lifetimes above 100 ps,” *The European Physical Journal C* **84** no. 6, (June, 2024) . <http://dx.doi.org/10.1140/epjc/s10052-024-12906-3>.

- [39] **LHCb** Collaboration, I. Bediaga, J. M. De Miranda, *et al.*, “Framework TDR for the LHCb Upgrade: Technical Design Report,” tech. rep., 2012. <https://cds.cern.ch/record/1443882>.
- [40] T. L. Collaboration, A. A. A. Jr, *et al.*, “The lhcb detector at the lhcb,” *Journal of Instrumentation* **3** no. 08, (Aug, 2008) S08005. <https://dx.doi.org/10.1088/1748-0221/3/08/S08005>.
- [41] **LHCb** Collaboration, “LHCb Trigger and Online Upgrade Technical Design Report,”.
- [42] **LHCb** Collaboration, “LHCb Tracker Upgrade Technical Design Report,”.
- [43] V. Kholoimov, B. K. Jashal, A. Oyanguren, V. Svintozelskyi, and J. Zhuo, “A downstream and vertexing algorithm for long lived particles (llp) selection at the first high level trigger (hlt1) of lhcb,” *Computing and Software for Big Science* **9** no. 1, (Jul, 2025) 10. <https://doi.org/10.1007/s41781-025-00141-8>.
- [44] L. collaboration, R. Aaij, *et al.*, “Long-lived particle reconstruction downstream of the lhcb magnet.” 2024. <https://arxiv.org/abs/2211.10920>.
- [45] **LHCb** Collaboration, “Dataflow diagrams for LHCb user analysis in Run 3 ,”. <https://cds.cern.ch/record/2896664>.
- [46] R. Aaij, S. Benson, *et al.*, “A comprehensive real-time analysis model at the LHCb experiment,” *Journal of Instrumentation* **14** no. 04, (2019) P04006–P04006.
- [47] R. Aaij, S. Amato, *et al.*, “Tesla: an application for real-time data analysis in High Energy Physics,” *Computer Physics Communications* **208** (2016) 35–42.
- [48] C. Fitzpatrick and V. V. Gligorov, “Anatomy of an upgrade event in the upgrade era, and implications for the LHCb trigger,”.
- [49] R. Aaij, J. Albrecht, *et al.*, “Allen: A high-level trigger on gpus for lhcb,” *Computing and Software for Big Science* **4** no. 1, (Apr., 2020) . <http://dx.doi.org/10.1007/s41781-020-00039-7>.
- [50] D. H. C. Pérez, N. Neufeld, and A. R. Núñez, “Search by triplet: An efficient local track reconstruction algorithm for parallel architectures,” *Journal of Computational Science* **54** (2021) 101422.
- [51] R. E. Kalman, “A new approach to linear filtering and prediction problems,”.
- [52] S. Aiola, Y. Amhis, *et al.*, “Hybrid seeding: A standalone track reconstruction algorithm for scintillating fibre tracker at LHCb,” *Computer Physics Communications* **260** (2021) 107713.

- [53] L. Calefice, “Standalone track reconstruction on GPUs in the first stage of the upgraded LHCb trigger system & Preparations for measurements with strange hadrons in Run 3.” 2022. <https://cds.cern.ch/record/2856339>. Presented 13 Dec 2022.
- [54] J.-P. Dedieu, “Newton-raphson method,” in *Encyclopedia of Applied and Computational Mathematics*, B. Engquist, ed., pp. 1023–1028. Springer Berlin Heidelberg, Berlin, Heidelberg, 2015.
https://doi.org/10.1007/978-3-540-70529-1_374.
- [55] **LHCb** Collaboration, “Discovery potential of LHCb Upgrade II,”
<https://cds.cern.ch/record/2921903>. - Contact: Tim Gershon, Frédéric Blanc, Phoebe Hamilton, Arantza De Oyanguren Campos, Giovanni Punzi, Vincenzo Vagnoni - Reviewers: Guy Wilkinson, Yasmine Amhis - Deadline for comments: 04/02/2025 - Reading Institutions: on a volunteer basis.
- [56] C. Antel, M. Battaglieri, *et al.*, “Feebly interacting particles: Fips 2022 workshop report.” 2023. <https://arxiv.org/abs/2305.01715>.
- [57] A. Boyarsky, M. Ovchinnikov, O. Ruchayskiy, and V. Syvolap, “Improved big bang nucleosynthesis constraints on heavy neutral leptons,” *Physical Review D* **104** no. 2, (July, 2021) . <http://dx.doi.org/10.1103/PhysRevD.104.023517>.
- [58] N. Sabti, A. Magalich, and A. Filimonova, “An extended analysis of heavy neutral leptons during big bang nucleosynthesis,” *Journal of Cosmology and Astroparticle Physics* **2020** no. 11, (Nov., 2020) 056–056.
<http://dx.doi.org/10.1088/1475-7516/2020/11/056>.
- [59] **LHCb** Collaboration, M. Clemencic, G. Corti, S. Easo, C. R. Jones, S. Miglioranza, M. Pappagallo, and P. Robbe, “The LHCb simulation application, Gauss: Design, evolution and experience,” *J. Phys. Conf. Ser.* **331** (2011) 032023.
- [60] LHCb Collaboration, “LHCb DecFiles Documentation,”
<https://lhcbdoc.web.cern.ch/lhcbdoc/decfiles/>, 2025. Accessed: 2025-06-30.
- [61] **LHCb** Collaboration, “BuSca: a Buffer Scanner at HLT1 using 2024 LHCb data,”
<https://cds.cern.ch/record/2914494>.
- [62] J. Podolanski and R. A. and, “Iii. analysis of v-events,” *The London, Edinburgh, and Dublin Philosophical Magazine and Journal of Science* **45** no. 360, (1954) 13–30, <https://doi.org/10.1080/14786440108520416>.
<https://doi.org/10.1080/14786440108520416>.

- [63] **LHCb** Collaboration, “BuSca: a Buffer Scanner at HLT1 to detect LLPs beyond the SM,”. <https://cds.cern.ch/record/2904666>.
- [64] Sjöstrand, Torbjörn and Utheim, Marius, “A framework for hadronic rescattering in pp collisions,” *Eur. Phys. J. C* **80** no. 10, (2020) 907.
<https://doi.org/10.1140/epjc/s10052-020-8399-3>.
- [65] **LHCb** Collaboration, “HLT1 Downstream performance in 2024 data-taking,”.
<https://cds.cern.ch/record/2914404>.
- [66] **LHCb** Collaboration, “Background study from BuSca: Insights from October 2024 LHCb data,”. <https://cds.cern.ch/record/2923556>.
- [67] M. Oreglia, “A Study of the Reactions $\psi' \rightarrow \gamma\gamma\psi$,” other thesis, 12, 1980.